Interdisciplinary Research in Medical Sciences Specialty
ISSN: 3062-4401
2025, Volume 5, Issue 2, Page No: 254-278

Available online at: www.galaxypub.co/page/journals

Galaxy Publication

Microneedle-Mediated Delivery of Ru Nanozyme–Magnesium Silicate Nanosheets Restores Redox and Regenerative Balance in Irradiated Skin

Omar Zayed[1]*, Leila Ibrahim[1], Ahmed Mansour[2]

[1]Department of Nanomedicine and Radiation Dermatology, Faculty of Medicine, Cairo University, Cairo, Egypt.
[2]Department of Wound Healing and Regenerative Medicine, Faculty of Medicine, Alexandria University, Alexandria, Egypt.

***E-mail** ✉ omar.zayed@cu.edu.eg

Received: 29 September 2025; **Revised:** 08 December 2025; **Accepted:** 18 December 2025

ABSTRACT

Radiotherapy-induced skin defect (RISD) represents a major adverse effect of radiation treatment, marked by prolonged oxidative stress and repeated overproduction of reactive oxygen species (ROS) that obstruct physiological tissue regeneration. The absence of a reliable standardized animal model, however, continues to impede advancement in this field. To address this issue, we propose an innovative strategy for remodeling the RISD microenvironment through a sequential process involving initial ROS neutralization, followed by suppression of further ROS formation and restoration of key cell proliferation pathways and functions. As proof of principle, we fabricated a composite microneedle (MN) patch using γ-polyglutamic acid as the supporting matrix and ruthenium (Ru) cluster-decorated magnesium silicate nanosheets (MSR NSs) as the bioactive enzyme-mimicking element. The incorporated Ru clusters display strong ROS-scavenging performance and activate the peroxisome proliferator-activated receptor signaling pathway, as demonstrated by transcriptomic sequencing. Concurrently, physiological degradation of the magnesium silicate component releases magnesium and silicate ions that promote cellular proliferation, migration, and new blood vessel formation. Using a radiation-induced skin defect animal model, we compared the reparative efficacy of the MSR@MN patch against both a γPGA-MSR ointment formulation and the commercial agent Orgotein. Results indicate that the MSR@MN patch successfully corrects the dysregulated microenvironment associated with excessive ROS, dampens inflammation, and facilitates mature vascularization along with effective tissue reconstruction.

Keywords: Microneedle patch, Radiotherapy induced skin defects, Ruthenium clusters, Skin repair

How to Cite This Article: Zayed O, Ibrahim L, Mansour A. Microneedle-Mediated Delivery of Ru Nanozyme–Magnesium Silicate Nanosheets Restores Redox and Regenerative Balance in Irradiated Skin. Interdiscip Res Med Sci Spec. 2025;5(2):254-78. https://doi.org/10.51847/aup2Nd00bs

Introduction

Radiation therapy serves as a critical intervention in oncology, utilizing high-energy radiation to destroy cancerous cells and forming part of standard care for roughly 70% of cancer patients worldwide. While generally regarded as safe and efficacious, it can provoke multiple side effects including nausea, vomiting, fatigue, skin damage, reduced blood cell counts, and, in more serious cases, radiation-induced lung injury or esophageal damage, all of which may adversely affect patient survival and well-being [1-5]. Among radiation-related complications, radiation-induced skin defects (Radiotherapy induced skin defect (RISD)), commonly termed radiation ulcers, pose particularly difficult management problems [6]. These lesions frequently arise during treatment of superficial cancers such as breast and head-neck malignancies, leading to deep tissue breakdown, large defects, profuse bleeding, systemic infection, and occasionally fatal outcomes [7, 8]. Therefore, the design of specialized wound dressings optimized for post-radiation RISD care is urgently needed to improve patient recovery.

Owing to its penetrating characteristics, ionizing radiation damages not only tumor cells but also nearby normal tissues, thereby establishing a disordered pathological and physiological milieu. This milieu is typified by

impaired mitochondrial function, overabundant production of reactive oxygen species (ROS) and free radicals, sustained oxidative damage, and repeated inflammatory activation [9-11]. Radiation exposure further perturbs multiple intracellular signaling cascades, upsetting the finely tuned regulation of cell growth, programmed cell death, and blood vessel development [12]. Consequently, strategies that effectively lower excessive ROS levels and reinstate normal signaling mechanisms disrupted by radiation are vital for correcting the RISD microenvironment. In response, extensive efforts have explored nanomaterials possessing intrinsic enzyme-like activities designed to mimic endogenous enzymes for ROS detoxification and dermal repair [13-19]. Conventional approaches to ROS clearance often rely on increasing material dosage to boost performance; however, many such catalytic agents exhibit dose-dependent toxicity that can harm healthy cells [20]. Thus, developing materials capable of potent ROS scavenging at minimal concentrations remains a key obstacle.

Ruthenium (Ru), a member of the platinum-group metals, is distinguished by its high catalytic efficiency, remarkable chemical stability, and strong performance under mild conditions. Its established roles in diagnostic reagents and anticancer agents attest to the reliability of its antioxidant capabilities [21-25]. These attributes position ruthenium as an attractive candidate for counteracting ROS-driven pathology in RISD at low doses.

Most existing research has emphasized ROS neutralization, yet comprehensive restoration of damaged skin architecture and function—including recovery of radiation-altered pathways such as p38 MAPK (mitogen-activated protein kinase), p53, JNK (c-Jun N-terminal kinase), and ERK1/2—has been insufficiently addressed [26, 27]. The limited bioactivity of current ROS-scavenging nanomaterials typically restricts their benefits to early hemostatic and inflammatory wound-healing stages, with minimal impact on later proliferative and remodeling phases [28-30]. Bioactive inorganic compounds therefore offer promising potential for reshaping the RISD microenvironment [31, 32]. Silicate materials, in particular, have demonstrated capacity to stimulate cell proliferation, support angiogenesis, and regulate inflammatory processes during tissue regeneration [33, 34]. Integrating ROS-scavenging nanomaterials with such bioactive components thus constitutes a compelling strategy for creating effective RISD repair systems that simultaneously mitigate oxidative stress and repair disrupted signaling networks.

Microneedle technology has gained attention in recent years for treating various wound types, including acute, chronic, infected, and burn injuries, due to advantages such as deep tissue penetration, secure anchoring, and convenient application [35, 36]. Unlike standard topical dressings or systemic delivery, microneedles bypass the skin barrier to provide both immediate and prolonged therapeutic release directly into the wound bed. Despite these benefits, their application to radiation-induced cutaneous injury has received relatively little investigation [37].

As shown in Scheme 1, the current work presents a composite microneedle (MN) patch that embeds ruthenium-loaded magnesium silicate nanosheets (MSR NSs) to achieve multifaceted RISD therapy through oxidative stress relief, ROS production control, and normalization of cellular signaling. Ultrathin magnesium silicate (MS) nanosheets were first prepared by a controlled solution-phase synthesis. Ruthenium ions were then adsorbed and reduced onto these nanosheets to yield MSR, imparting potent antioxidant properties that neutralize ROS, limit its continued generation, and safeguard cellular functions. The resulting MSR was incorporated into a γ-polyglutamic acid (γ-PGA) matrix via solvent casting to produce the MSR@MN patch. This design leverages microneedle strengths—efficient barrier penetration, precise localization, and direct cargo delivery—to the injured site. Both in vitro and in vivo assessments examined the impact of percutaneous MSR administration on ROS elimination, re-epithelialization, vessel formation, collagen synthesis, and hair follicle recovery. Comparative evaluation against the commercial product Orgotein was performed in animal models to highlight potential advantages. Overall, this approach offers a valuable new avenue for RISD management that surmounts shortcomings of conventional therapies and enhances patient outcomes and quality of life.

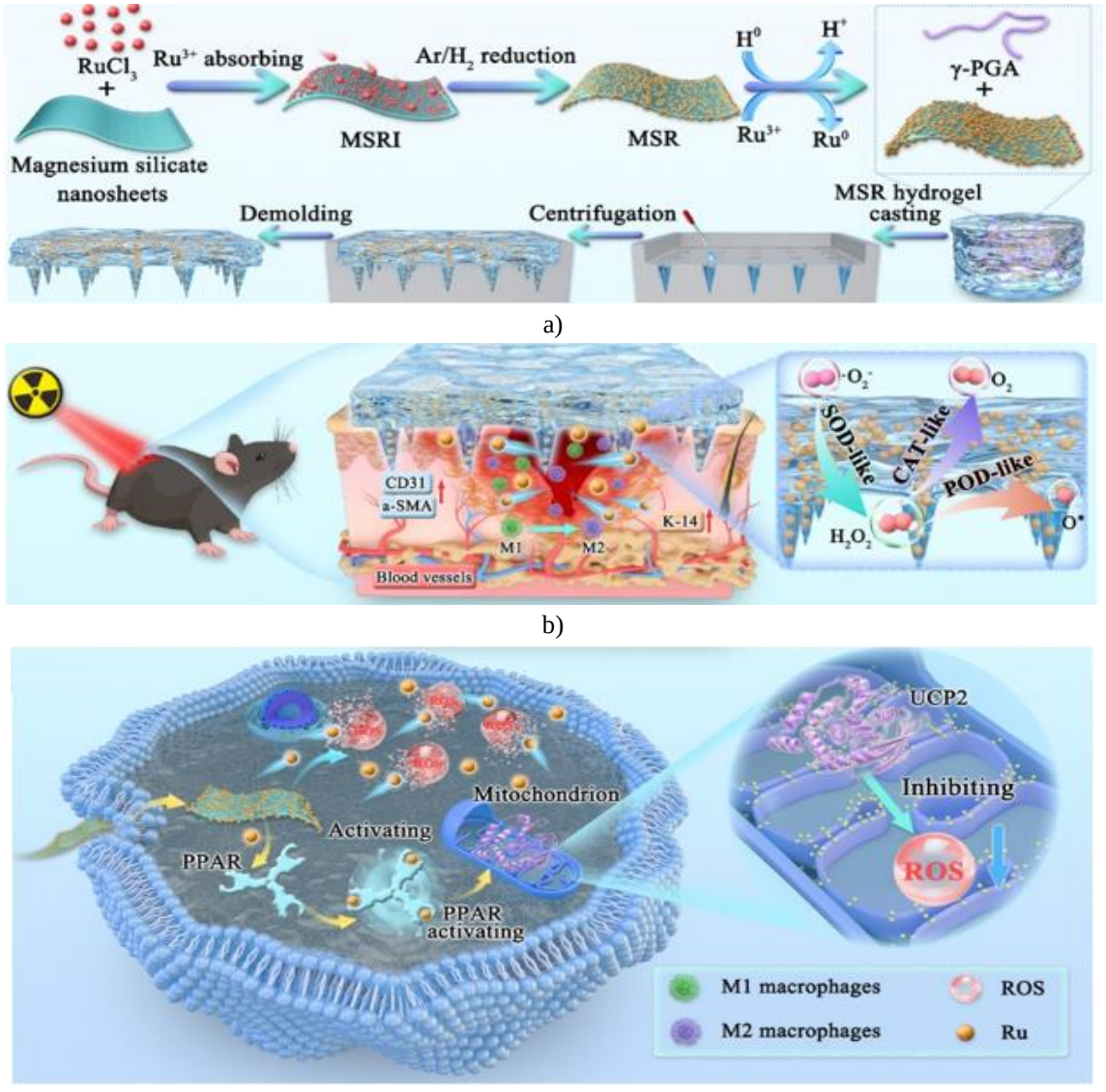

Scheme 1. Schematic representation of the fabrication and therapeutic application of the MSR@MN patch for radiation-induced skin defects. (a) Preparation and characterization of MSR@MN. (b) MSR@MN modulates the full healing cascade of RISD in mice. (c) Cellular-level free-radical-scavenging capability of MSR@MN.

Materials and Methods

$Na_2SiO_3 \cdot 9H_2O$, $MgCl_2$, and $RuCl_3 \cdot xH_2O$ were acquired from Aladdin Industrial Co., Ltd (Shanghai, China). Commercial assay kits including CCK-8, ROS Assay Kit, Trypsin-EDTA solution, Cell Live/Dead staining kit, Paraformaldehyde Fix Solution, and Phosphate Buffered Saline (PBS) were supplied by Beyotime (Shanghai, China). Matrigel Matrix originated from Corning Incorporated (New York, USA). The magnesium ion detection kit was obtained from Saint Biotechnology Co., Ltd (Shanghai, China), while the hydroxyl radical detection kit came from Nanjing Jiancheng Biotechnology Co., Ltd (Nanjing, China). Orgotein was procured from Jianpu Biotechnology Co., Ltd (Wuxi, China).

Preparation of MS nanosheets

In brief, $Na_2SiO_3 \cdot 9H_2O$ (0.85 mg) was first dissolved in 50 mL of deionized water. A 5.0 mL portion of $MgCl_2$ aqueous solution (0.6 M) was then added dropwise at a steady rate of 2.5 mL h^{-1} while the mixture was magnetically stirred at room temperature. Stirring continued for 3 h after complete addition of the magnesium

salt. The formed precipitate was isolated by centrifugation, washed repeatedly (three times) with deionized water and absolute ethanol, and finally dried under vacuum conditions for 24 h.

Preparation of Ru-functionalized MS (MSR) nanosheets

MS nanosheets (20 mg) were uniformly dispersed in 14 mL of an ethanol solution containing $RuCl_3 \cdot xH_2O$ (10.3 mg) and stirred overnight at ambient temperature. The solvent was subsequently evaporated by oven drying at 50°C, yielding MS material loaded with Ru^{3+} ions (denoted as MSRI). Reduction of the adsorbed ruthenium ions was performed by heating the MSRI sample at 250°C for 2 h under a 5% H_2/Ar atmosphere to generate the final Ru-functionalized MS nanosheets.

Materials characterization

Structural morphology and composition were investigated using scanning electron microscopy (SEM, ZEISS GeminiSEM 300, Germany), Raman spectroscopy (Renishaw inVia, UK), and optical microscopy (Nikon Corporation, Japan). Surface elemental analysis and chemical bonding information were obtained through X-ray photoelectron spectroscopy (XPS, Thermo Scientific ESCALAB Xi+, USA) and X-ray diffraction (XRD, Rigaku Ultima IV, Japan).

Peroxidase-like activity of nanozymes

Evaluation of peroxidase-mimicking catalytic activity was conducted at room temperature. The reaction mixture consisted of magnesium silicate nanosheets (20 μg mL^{-1}), H_2O_2 (0.5 mM), and 3,3',5,5'-tetramethylbenzidine (TMB, 0.5 mM) in 1 mL of NaAc buffer (pH 5.2, 0.1 M). Enzyme kinetics were studied by varying the concentration of one substrate (MSR or H_2O_2) while holding the other at a fixed level (0.5 or 1 mM for H_2O_2; 0.5 or 1 mM for TMB). Changes in solution absorbance were recorded with a UV-Vis spectrophotometer.

Catalase activity assays

MSR at a concentration of 150 μg mL^{-1} was introduced into a phosphate buffer (pH 7.4, 1X) containing 1 M H_2O_2. The reaction was monitored continuously for 300 s at 25°C using a UV-Vis spectrometer operating in kinetic mode to follow absorbance variations.

Synthesis of fluorescein isothiocyanate-MSR (FITC-MSR)

Fluorescent labeling was achieved by first preparing a FITC conjugate. FITC (4 mg), sodium hydroxide (400 mg), and 3-(azidopropyl)triethoxysilane (500 μL) were combined in 5 mL absolute ethanol and allowed to react for 24 h at room temperature while protected from light. The resulting solution (20 mL) was then mixed with MSR (50 mg) for 12 h. The labeled product was washed with 95% ethanol and vacuum-dried. For uptake studies, NIH/3T3 cells were plated at 1×10^5 cells per well in 6-well plates, cultured overnight, and subsequently exposed to 10 μg/mL FITC-MSR. Intracellular localization was observed via fluorescence microscopy.

Assessment of mg and Ru release profiles

To investigate ion release behavior, 6 mg of MSR was placed in 2 mL of deionized water and incubated at 37°C with gentle shaking. At scheduled intervals (1, 3, 5, 7, 9, 11, 13, and 15 days), 1 mL aliquots were removed and replaced with fresh deionized water. Magnesium concentrations were determined using a commercial magnesium detection reagent kit (Saint-Bio, Shanghai). Ruthenium levels were quantified by inductively coupled plasma atomic emission spectroscopy (ICP, Agilent 720ES, USA).

Fabrication and characterization of MN patch

Microneedle molds were obtained from New Material Technology Co., Ltd (Anhui, China). Separate γ-PGA hydrogels containing MSR, MS, or no additional filler were dispensed into the molds, centrifuged at 2000 rpm for 5 min to ensure complete filling, and excess hydrogel was removed from the surface. The molds were then dried in a 37°C oven for 6 h. Optical microscopy was employed to capture images of the resulting microneedle arrays with different loadings.

Mechanical strength test

Mechanical performance of the microneedle patches was evaluated on a universal testing machine (Instron 3343, USA) fitted with a 1000 N load cell. The test configuration maintained an initial 3 mm gap between the

microneedle tips and a stainless steel compression plate. The plate advanced at 2 mm min^{-1} toward the patch, and force-displacement curves were recorded throughout the compression process.

Free-radical-scavenging capability of MSR

Antioxidant capacity was assessed using multiple standard assays: 2,2-diphenyl-1-picrylhydrazyl (DPPH) radical scavenging, 2,2′-azino-bis(3-ethylbenzthiazoline-6-sulfonic acid) (ABTS) radical cation decolorization, and hydroxyl radical (•OH) scavenging. Additional confirmation of •OH, $^1O_2$, and O_2^{-}• elimination was obtained via electron spin resonance (ESR) spectroscopy. In the DPPH assay, equal volumes of MSR solutions at different concentrations and DPPH ethanol solution (0.04 mg/mL) were combined and kept in the dark for 30 min, followed by absorbance measurement at 519 nm. For the ABTS assay, radicals were pre-generated by incubating 7.4 mmol/L ABTS with 2.6 mmol/L potassium persulfate in darkness for 24 h. The test involved mixing 0.6 mL MSR solution with 2.4 mL ABTS radical solution for 10 min before reading absorbance at 734 nm. The •OH scavenging procedure adhered to the manufacturer's protocol for the commercial kit. Prior to UV-Vis analysis, all reaction mixtures were centrifuged (10,000 rpm, 10 min) to eliminate residual MSR particles. Experiments were conducted in triplicate. Scavenging efficiency was determined using the formula: Scavenging rate (%) = $(A_0 - A)/A_0$, where A_0 is the absorbance of the control without MSR and A is the absorbance measured in the presence of MSR.

The ability of MSR to eliminate •OH, $^1O_2$, and O_2^{-}• species was further verified by ESR spectroscopy. •OH radicals were generated through the Fenton reaction, singlet oxygen ($^1O_2$) via titanium dioxide photocatalysis, and superoxide (O_2^{-}•) using the xanthine/xanthine oxidase system. 2,2,6,6-Tetramethylpiperidine was employed as the spin trap for $^1O_2$ detection, whereas 5,5-dimethyl-1-pyrroline-N-oxide served as the trapping agent for both •OH and O_2^{-}•.

Extracts preparation

MS and MSR extracts were generated in accordance with the International Organization for Standardization recommendations. Specifically, the materials were immersed in culture medium at a ratio of 200 mg per mL and maintained at 37°C for 24 h. The resulting suspensions were centrifuged at 1600 rpm for 10 min and passed through 0.22 μm filters. Serial dilutions of the clarified extracts were then prepared using basal culture medium as required for subsequent testing.

Cell culture assays

NIH/3T3 cells and human umbilical vein endothelial cells (HUVECs) were sourced from the Cell Bank of the Chinese Academy of Sciences (Shanghai, China). These cell lines were routinely propagated in Dulbecco's modified Eagle medium containing 10% fetal bovine serum and 1% penicillin-streptomycin mixture, under standard conditions of 5% CO_2 in a humidified incubator.

Radiation damage model in cells induced by ray irradiation

Once HUVECs and NIH/3T3 cells had attached, they were irradiated at graded doses (0, 2, 4, 6, 8, 10, and 12 Gy) delivered by a linear accelerator (Varian Clinac iX, USA). Twenty-four hours later, cell viability was evaluated with the CCK-8 assay. The radiation dose chosen for further experiments on both cell types was that which produced roughly a 50% decrease in viability relative to non-irradiated controls.

Cytotoxic effect of extracts

Potential toxicity of the extracts was determined by CCK-8 assay to identify safe working concentrations. Irradiated cells were plated at 5000 cells per well in 96-well plates and allowed to adhere overnight. Various dilutions of the extracts were then applied, followed by addition of CCK-8 reagent as specified by the manufacturer. Absorbance readings were obtained using a microplate reader (Thermo Fisher, USA).

Reactive oxygen species scavenging detection

Cells were seeded into 24-well plates and pretreated overnight with selected extract dilutions. Following irradiation, incubation continued for 4 h before addition of 2′,7′-dichlorodihydrofluorescein diacetate (DCFH-DA) and the JC-1 Mitochondrial Membrane Potential Assay Kit (Beyotime) according to the provided protocols. Fluorescence corresponding to 2′,7′-dichlorofluorescein (DCF) and JC-1 was imaged after approximately 20 min using a fluorescence microscope. Fluorescence intensity was quantified with ImageJ software.

In vitro cytocompatibility and proliferation test

Irradiation of cells was performed as outlined above. Cytocompatibility was examined via live/dead staining following the kit instructions. Cells were seeded at 2×10^5 cells per well in 24-well plates, cultured overnight, and exposed to different extract concentrations. After 30 min staining, fluorescence images were acquired. Normal culture medium served as the untreated control, with all groups tested in triplicate. Proliferation capacity was measured using the CCK-8 assay per manufacturer guidelines. Cells were plated at 3000 cells per well, allowed to attach overnight, and incubated with extract dilutions for 1, 2, or 3 days. Absorbance at 450 nm was recorded on a microplate reader, with experiments repeated in triplicate.

Scratch tests

Cell migratory behavior was investigated using a scratch wound assay. Cells were grown in 6-well plates until reaching approximately 90% confluence after 24 h. Following radiation treatment, a uniform scratch was introduced with a 200 μL pipette tip. Cultures were then maintained in medium containing different extracts, with PBS-treated wells as controls. After 24 h, microscopic images were taken, and the remaining scratch area was analyzed with ImageJ software. Wound closure was calculated according to the formula: scratch healing% = $(S_0 - S_t)/S_0 \times 100\%$, where S_0 is the initial wound area and S_t is the area measured at time t.

Migration and tube formation

Transwell chambers in 24-well plates were utilized to assess HUVEC migration. Cells were placed in the upper compartment, while extract solutions occupied the lower chamber. After 24 h, non-migrated cells were gently removed from the upper surface using a cotton swab. Migrated cells on the underside were fixed with paraformaldehyde, stained with crystal violet, photographed under bright field, and counted. For evaluation of angiogenic potential, 96-well plates were coated with 50 μL Matrigel matrix (Corning, NY, USA). HUVECs (2×10^4 cells in 100 μL) were seeded onto the solidified matrix and incubated for 4 h. Tube formation was quantified by measuring the number of nodes and total tube length using ImageJ software.

Hemolysis assay

Mouse red blood cell suspensions were mixed with MN, MS@MN, or MSR@MN patches and incubated at 37°C for 2 h. Positive and negative controls consisted of erythrocytes suspended in deionized water and PBS, respectively. After incubation, samples were centrifuged at 1200 rpm for 10 min. Visual inspection of hemolysis was documented photographically. One hundred microliters of supernatant were transferred to 96-well plates, and absorbance was measured at 540 nm. The hemolysis percentage was computed using the equation: Hemolysis rate $(\%) = (A_{test} - A_{neg})/(A_{pos} - A_{neg}) \times 100\%$, where A_{test}, A_{pos}, and A_{neg} represent the absorbance readings of the test sample, positive control, and negative control, respectively.

Radiation-induced skin defects model

All animal experiments complied strictly with NIH recommendations regarding laboratory animal welfare and received approval from the Animal Ethics Committee of Shanghai 10th People's Hospital, affiliated with Tongji University School of Medicine (approval number: SHDSYY-2024-T0102). Male C57/BL mice aged 6 weeks (purchased from B and K Universal Ltd., China) were anesthetized via intraperitoneal administration of 3% pentobarbital sodium at a dose of 30 mg kg^{-1}, after which dorsal hair was carefully shaved. The animals were then randomly allocated into several experimental groups: Sham, Control, MN, MS@MN, MSR@MN, γPGA-MSR ointment, and Orgotein. No radiation exposure was applied to the Sham group. For the other groups, a defined area of buttock skin measuring 8 × 8 mm was subjected to a single localized radiation dose of 30 Gy. Seven days later, when signs of skin damage such as erythema, desquamation, and mucosal disruption appeared, standardized full-thickness circular excisional wounds of 8 mm diameter were surgically created on the irradiated sites. A stainless-steel ring (inner diameter 8 mm, outer diameter 16 mm, thickness 1 mm) was placed over each wound and fixed firmly to the surrounding skin using medical adhesive and sutures. This ring served to maintain wound patency and prevent skin contraction or premature closure. Digital photographs of the wounds were acquired on days 3, 7, 10, and 12, with wound areas quantified using ImageJ software. Wound closure rates were determined using the equation: wound closure rate $(\%) = (S_0 - S_t) / S_0 \times 100\%$, where S_0 is the original wound area measured on day 0 and S_t corresponds to the area at each specified time point.

Histological analysis

At days 3 and 12 post-treatment, animals were euthanized, and wound tissues along with surrounding normal skin and major organs (heart, lung, liver, spleen, kidney) were collected. Both frozen and paraffin-embedded sections were prepared. Frozen sections underwent staining with a dedicated ROS detection kit. General tissue morphology and repair status were examined through hematoxylin and eosin (H&E) staining. Collagen content was evaluated using Masson's trichrome staining. Immunofluorescence techniques were applied to characterize macrophage phenotypes, re-epithelialization extent, and new vessel formation. Macrophage subtypes were labeled with CD86 and CD206 antibodies, combined with 4',6-diamidino-2-phenylindole for nuclear visualization. Epithelial layer thickness was assessed by CK14 staining, while vascular structures were identified using CD31 and α-SMA markers. Major organs were processed with H&E staining to screen for potential toxicity. Quantitative immunohistochemical evaluation was based on analysis of three randomly chosen microscopic fields per specimen from each experimental group.

Statistical analysis

Results are reported as mean ± standard deviation (SD). All experiments were performed at least three independent times with technical replicates ($n \geq 3$). Statistical significance was evaluated by unpaired Student's t-test or one-way analysis of variance using Statistical Product and Service Solutions software (version 25.0, IBM). Differences with $p < 0.05$ were considered statistically significant, whereas $p < 0.01$ and $p < 0.001$ denoted highly significant changes.

Results and Discussion

Synthesis and characterization of magnesium silicate nanosheets

Magnesium silicate (MS) nanosheets were synthesized via a solution precipitation process regulated by reaction kinetics. Ruthenium-loaded MS nanosheets possessing antioxidant capabilities were subsequently produced by means of a reduction process carried out in an Ar/H_2 atmosphere **(Figure 1a)**.

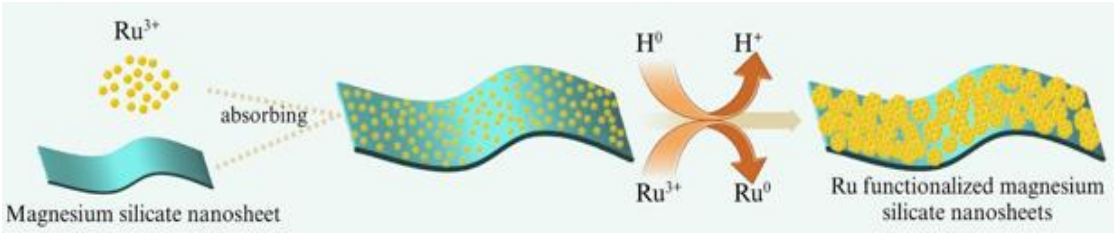

a)

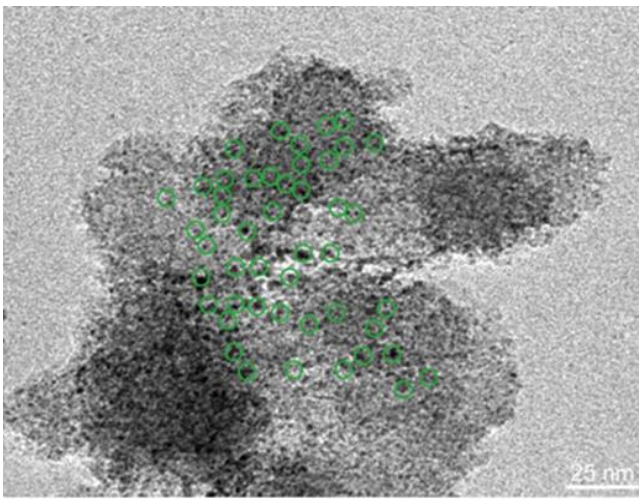

b)

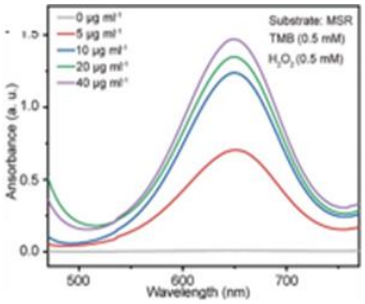

c)

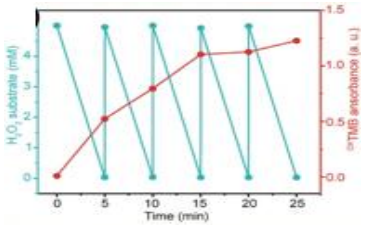

d)

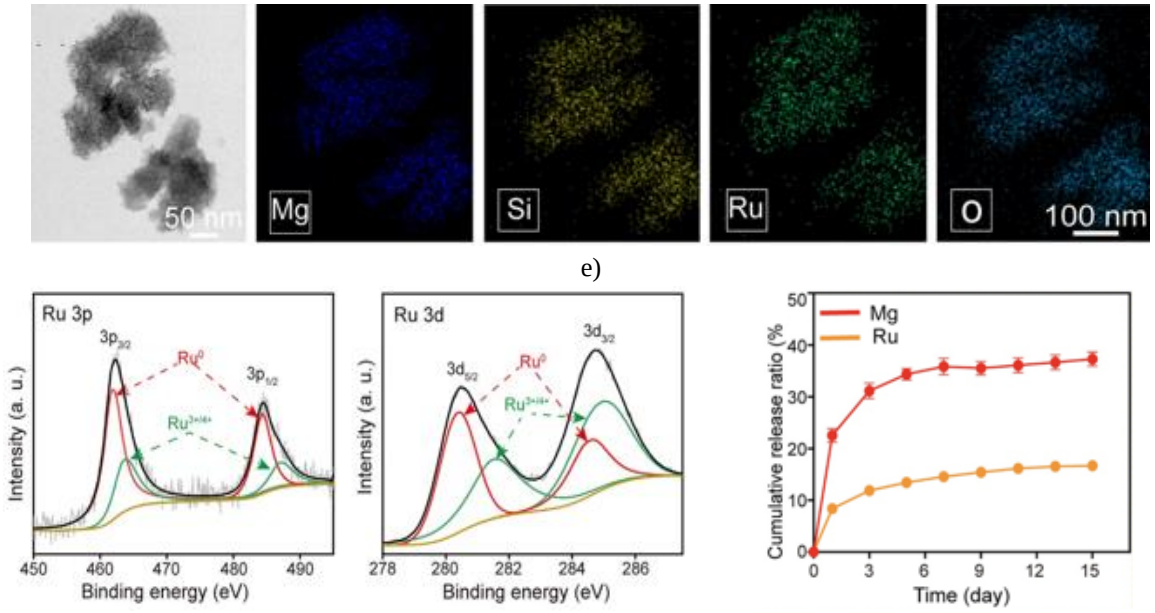

Figure 1. Characterization of ruthenium-loaded magnesium silicate nanosheets (MSR). (a) Schematic representation of the MSR synthesis procedure. (b) TEM images of MSR. (c) UV/Vis absorption spectra recorded for MSR at different concentrations. (d) Evaluation of H_2O_2 depletion and oxidized TMB (OXTMB) formation. (e) EDS mapping images of MSR specimens. (f) High-resolution Ru 3p and 3d XPS spectra of MSR. (g) Release curves of Mg and Ru from MSR.

The morphology of the obtained materials was investigated using transmission electron microscopy (TEM). The MS sample comprised flexible ultrathin nanosheets that assembled into a porous network. Ruthenium clusters appeared as dark nanoparticles on the nanosheet surfaces, marked with green circles **(Figure 1b)**. Energy-dispersive X-ray spectrometry (EDS) elemental mapping demonstrated the homogeneous distribution of Mg, Si, and Ru throughout the nanosheets. Quantitative elemental analysis by inductively coupled plasma mass spectrometry (ICP-MS) indicated Ru and Mg contents of 141.3 and 95.9 ppm in MSR, respectively, thereby substantiating the effective incorporation of ruthenium **(Figures 1b and 1e)**.

Structural features were examined first by X-ray diffraction (XRD). The MS sample displayed a broad diffraction maximum around 26.2°, characteristic of an amorphous component, along with reflections at 35.5° and 59.8° matching the tetragonal phase of magnesium silicate (PDF#00-047-1750). In the MSR pattern, an intense peak emerged at 43.7°, assignable to the hexagonal phase of metallic ruthenium (PDF#01-071-3766), which verified the generation of zero-valent Ru. Complementary Raman spectroscopic analysis was conducted. Pristine MS exhibited typical bands associated with Si–O–Si bending at 670 cm^{-1} and Si–O stretching at 1075 cm^{-1} [38, 39]. In MSR, these signals were largely suppressed by new features at 509 and 626 cm^{-1}, leaving only a weak shoulder near 684 cm^{-1}, an effect ascribed to ruthenium doping.

Ruthenium has received considerable interest for biomedical uses because of its varied enzyme-mimicking catalytic functions. These activities are governed by the element's oxidation state and structural configuration. Ru single atoms, mainly in higher oxidation states (+3 and +4), display peroxidase-like (POD-like) and superoxide dismutase-like (SOD-like) properties [25]. By contrast, Ru nanoparticles in the metallic (0) state predominantly manifest catalase-like (CAT-like) behavior together with strong antioxidant capacity [40]. Such versatile catalytic profiles are especially advantageous for controlling complex microenvironments involving radiation-induced oxidative stress. The oxidation of TMB by H_2O_2 in the presence of peroxidase produces blue-colored oxidized TMB (OXTMB) with peak absorbance at 652 nm. The POD-like performance of the materials was initially tested with the TMB/H_2O_2 system. Upon addition of MSR, a rapid and substantial rise in absorbance was recorded **(Figure 1c)**, revealing pronounced POD-like activity. Pure $MgSiO_3$, however, produced virtually no change, indicating minimal activity in this regard. Importantly, MSR demonstrated sustained catalytic efficiency, rapidly consuming H_2O_2 and oxidizing TMB across five successive cycles within 5 minutes per cycle **(Figure 1d)**. CAT-like activity was also confirmed: introduction of MSR led to a sharp decline in absorbance at 240 nm and the evolution of gas bubbles, consistent with H_2O_2 breakdown **(Figure 1d)**.

X-ray photoelectron spectroscopy (XPS) provided insight into the surface chemistry and electronic states of MSR. Survey spectra confirmed the presence of Mg, Si, Ru, O, and C, supporting successful ruthenium loading on the MS nanosheets. Detailed analysis of the Ru 3p region showed doublets at 462.3 and 484.4 eV, reflecting contributions from both Ru^{3+} and Ru^{0}. Dominant components at 461.9 and 484.4 eV corresponded to the $3p_{3/2}$ and $3p_{1/2}$ levels of metallic Ru, indicating effective reduction to the zero-valent state. Likewise, the Ru 3d spectrum displayed peaks at 280.5 and 284.8 eV, with the main signals at 280.4 and 284.5 eV aligning with Ru $3d_{5/2}$ and Ru $3d_{3/2}$ of Ru^{0}. These observations establish that metallic ruthenium was successfully formed and serves as the primary active species for radical scavenging in MSR **(Figure 1f)**. Ion release studies in deionized water revealed that Mg and Ru concentrations rose quickly over the first 3 days before stabilizing by day 6 **(Figure 1g)**. Cellular internalization was visualized by fluorescence microscopy in NIH/3T3 cells, where FITC-labeled MSR was readily detected in the perinuclear cytoplasmic region, confirming effective uptake. Given these release kinetics, MSR is expected to liberate Mg and Ru ions progressively during the initial wound healing phase, thereby modulating the ROS-enriched inflammatory milieu induced by radiotherapy and facilitating improved tissue repair.

Synthesis and characterization of MSR@MN

The γ-PGA hydrogel was selected as the foundational material for fabricating the microneedle (MN) patch owing to its favorable biodegradability, biological compatibility, and robust mechanical integrity following freeze-drying. These attributes facilitate effective dermal penetration by the needles, enabling controlled drug delivery. In addition, the MN patch base functions as a wound dressing that maintains a moist environment at the wound site, thereby supporting accelerated healing [41]. The multifunctional MSR@MN patch, featuring a 16 × 16 needle array, was prepared through a straightforward one-step template replication technique **(Figures 2a and 2b)**. Scanning electron microscopy (SEM) images revealed that the microneedles exhibited a pyramidal geometry. This sharp pyramidal design allows for rapid, minimally invasive, and precise insertion into deeper skin layers **(Figure 2c)**. Elemental mapping via energy-dispersive X-ray spectrometry (EDS) further confirmed the uniform incorporation of MSR within the MSR@MN patch **(Figure 2d)**.

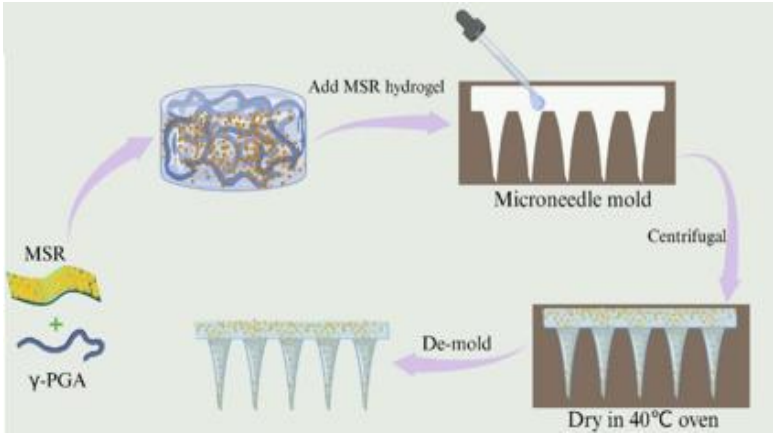

a)

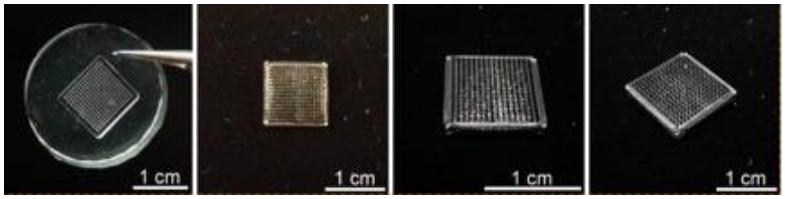

b)

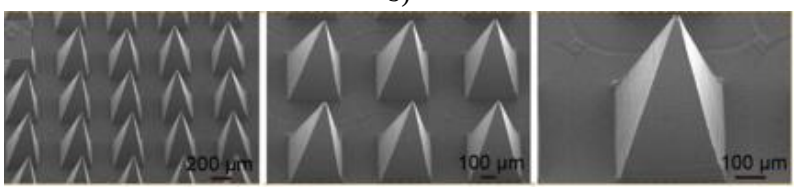

c)

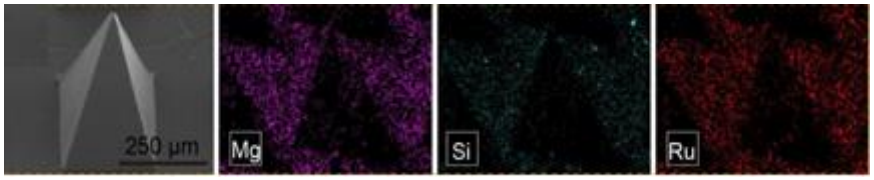

d)

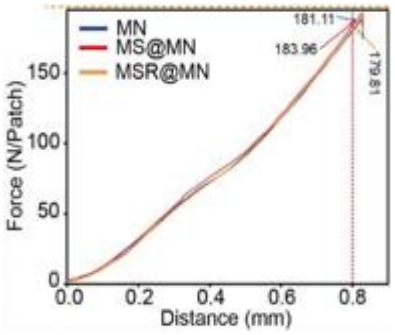

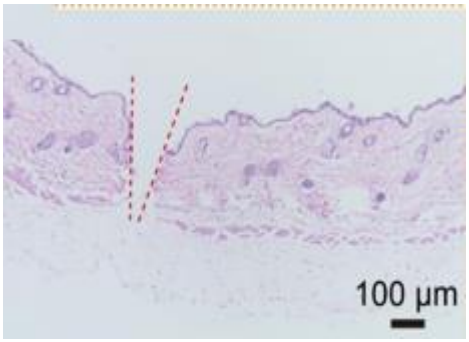

e) f)

Figure 2. Fabrication and characterization of MSR@MN. (a) Schematic depiction of the MSR@MN preparation process. (b) Optical photograph of the polydimethylsiloxane (PDMS) MN mold and the resulting MSR@MN patch. (c, d) SEM image (c) and energy-dispersive X-ray spectrometry (EDS) mapping (d) of MSR@MN. (e) Mechanical compression strength profiles of MN, MS@MN, and MSR@MN. (f) Histological image demonstrating penetration of MSR@MN into the skin dermis.

The SEM and EDS analyses were performed with the sample tilted at a 30-degree angle relative to the horizontal plane to collect secondary electrons. Consequently, only the lateral projection of the sample was visible in the elemental distribution maps. Mechanical testing demonstrated that the MN, MS@MN, and MSR@MN patches possess substantial mechanical strength, with maximum compressive forces of 0.695, 0.721, and 0.702 N, respectively. These values markedly exceed the minimum threshold of 0.045 N necessary for piercing the stratum corneum **(Figure 2e)** [42]. Ex vivo skin penetration experiments confirmed that the MSR@MN patch effectively reaches the dermis layer, enabling sustained drug release **(Figure 2f)**.

To confirm efficient payload delivery from the microneedle tips into the subcutaneous tissue, Rhodamine B was employed as a model compound and agarose hydrogel served as a skin mimic. The diffusion of the dye from the needle tips was monitored using laser confocal microscopy to reconstruct three-dimensional distribution profiles. The resulting images displayed extensive red fluorescence surrounding the needle insertion sites, demonstrating rapid release and diffusion of the payload from the microneedle tips into the surrounding hydrogel matrix.

Free-radical scavenging capabilities of magnesium silicate nanosheets

The microenvironment associated with radiation-induced skin damage (RISD) exhibits substantial accumulation of reactive oxygen species (ROS), which inflicts injury on adjacent healthy cells and tissues. This oxidative stress contributes to impaired wound healing and, in severe cases, chronic non-healing wounds [43]. Leveraging the superior catalytic properties of ruthenium, which readily engages in redox reactions with oxidants such as reactive oxygen and nitrogen species (ROS/RNS) [44], the antioxidant performance of MSR was systematically evaluated through DPPH and ABTS radical scavenging assays. MSR exhibited robust free-radical scavenging capacity against both radicals in a concentration-dependent manner. Notably, even at a relatively low concentration of 10 μg mL^{-1}, MSR achieved approximately 80% scavenging efficiency toward DPPH radicals **(Figures 3a and 3d)**. Comparable dose-dependent behavior was observed in the ABTS assay. At 70 μg mL^{-1}, MSR displayed only 7% clearance efficiency for ABTS; however, this value increased markedly to 85.1% when the concentration was raised to 120 μg mL^{-1} **(Figures 3b and 3e)**.

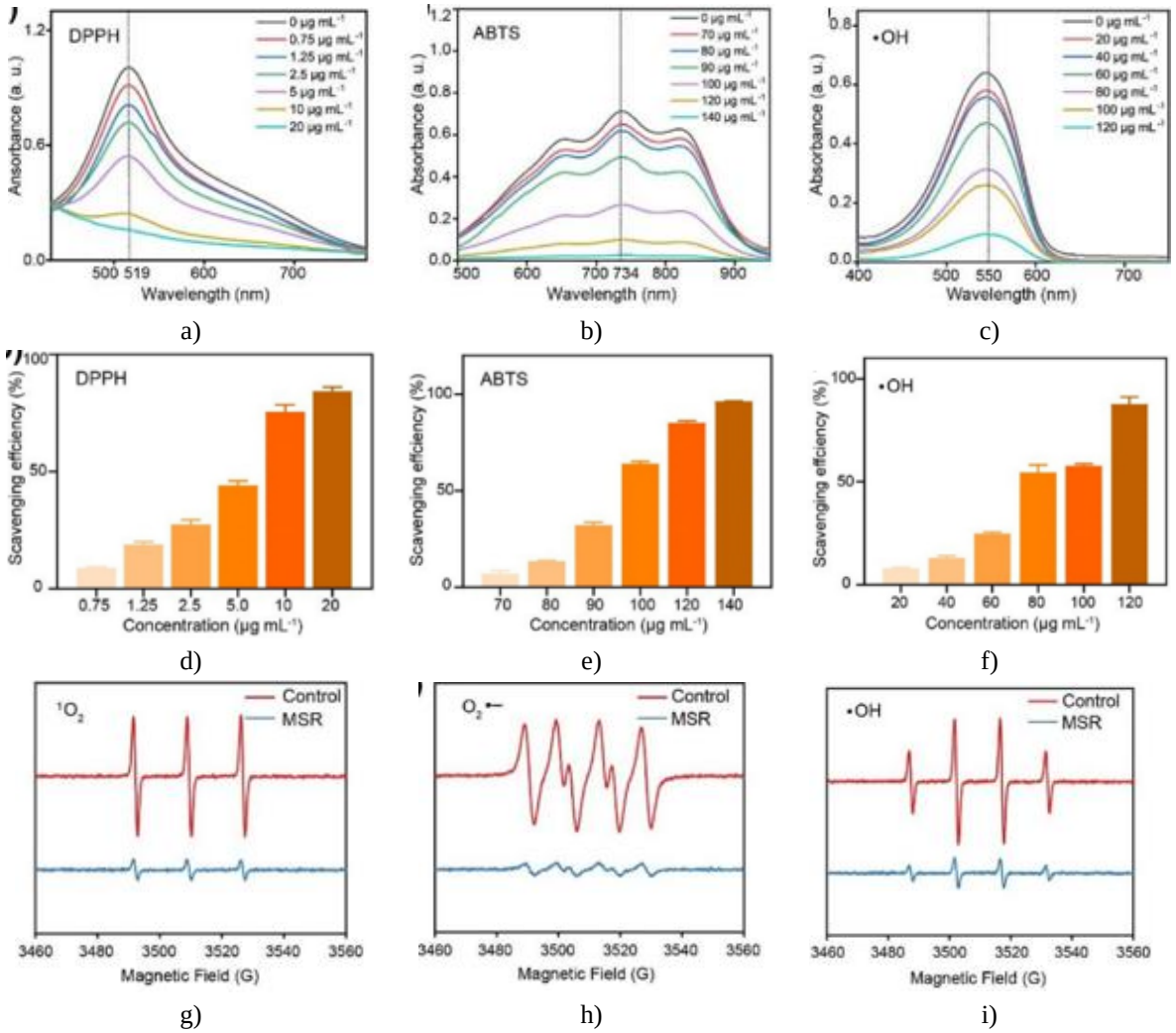

Figure 3. Free-radical scavenging performance of magnesium silicate nanosheets (MSR). (a–f) Scavenging activity of MSR against three representative free radicals: (a, d) 2,2-diphenyl-1-picrylhydrazyl radical (DPPH), (b, e) 2,2′-azino-bis(3-ethylbenzthiazoline-6-sulfonic acid) radical cation (ABTS), and (c, f) hydroxyl radical (•OH). (g–i) Electron spin resonance (ESR) spectra recorded after MSR incubation with (g) $^1O_2$, (H) $O_2^{\bullet-}$, and (I) •OH. All data are presented as mean ± standard deviation (SD).

Beyond DPPH and ABTS, the ability of MSR to neutralize hydroxyl radicals (•OH) was examined using a dedicated •OH assay kit **(Figures 3c and 3f)**. The quantified scavenging efficiencies reached 54.5% and 87.8% at concentrations of 80 and 120 μg mL^{-1}, respectively. In contrast, unmodified MS showed negligible radical scavenging activity at equivalent concentrations, confirming that the pronounced antioxidant effect of MSR originates from the ruthenium clusters anchored on the MS nanosheets. To further assess intracellular ROS clearance, representative species—including singlet oxygen ($^1O_2$), superoxide anion ($O_2^{\bullet-}$), and •OH—were investigated via electron spin resonance (ESR) spectroscopy **(Figures 3g–3i)**. The ESR spectra revealed a sharp reduction in the signal intensity of the characteristic peaks for $^1O_2$, $O_2^{\bullet-}$, and •OH following MSR treatment, highlighting its potent and broad-spectrum ROS scavenging capability. Collectively, these findings establish MSR as an effective antioxidant material capable of efficiently eliminating both ROS and RNS.

Cyto-protective, cytotoxicity, and biocompatibility of MSR@MN in vitro

Human umbilical vein endothelial cells (HUVECs) and rat fibroblast NIH/3T3 cell lines were utilized as in vitro models to evaluate the biocompatibility of MSR@MN, given their critical involvement in wound repair mechanisms. Initially, both cell types were exposed to different radiation doses to identify an appropriate experimental range. The radiation levels selected for HUVECs (8 Gy) and NIH/3T3 cells (6 Gy) were reduced by approximately 50% from preliminary viability tests to maintain adequate cell survival. Cells were then incubated with extracts of MSR@MN at a 1/16 dilution. Under these conditions, cell viability remained close to 100%,

indicating negligible cytotoxicity. Accordingly, the 1/16 dilution was selected as the working concentration for all subsequent in vitro assessments (Supporting Information S1). This strategy ensures both biological relevance and safety of the MSR@MN material for wound healing applications.

Radiation-induced cellular injury primarily stems from excessive production and buildup of reactive oxygen species (ROS). To confirm the ROS-scavenging capacity of MSR@MN, intracellular ROS levels were measured using the DCFH-DA probe. This indicator is oxidized by ROS to generate the green fluorescent product 2′,7′-dichlorofluorescein, with fluorescence intensity correlating directly with ROS abundance. It should be noted that cells naturally maintain a low basal level of ROS under normal conditions to support essential metabolic and signaling functions [45]. Non-irradiated cells served as controls representing physiological ROS levels. Following irradiation, enhanced green fluorescence was observed in the Control, MN, and MS@MN groups, reflecting elevated intracellular ROS. In marked contrast, the MSR@MN-treated group showed no substantial increase in fluorescence; instead, the intensity returned to levels comparable to those of non-irradiated cells **(Figures 4a, 4e and 4f)**. Excessive ROS can also disrupt mitochondrial membrane potential, leading to impaired respiratory function, amplified oxidative stress, and eventual cellular dysfunction. Treatment with MSR@MN significantly prevented the radiation-induced loss of mitochondrial membrane potential. These results clearly illustrate that MSR@MN effectively neutralizes intracellular ROS, thereby protecting cells from oxidative damage.

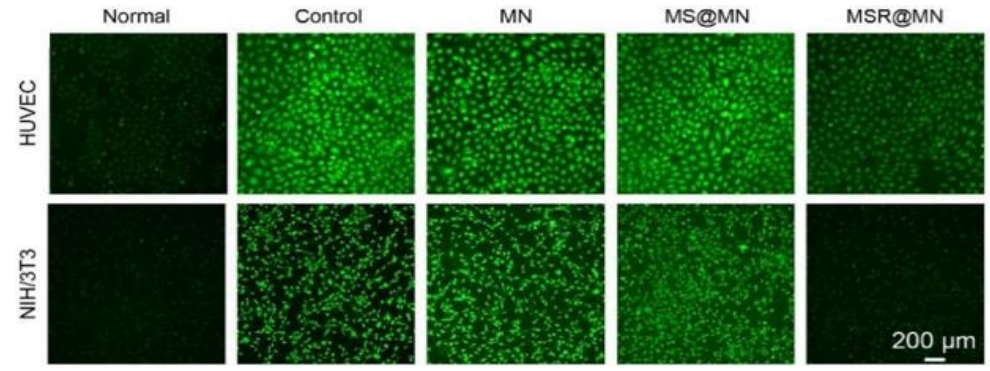

a)

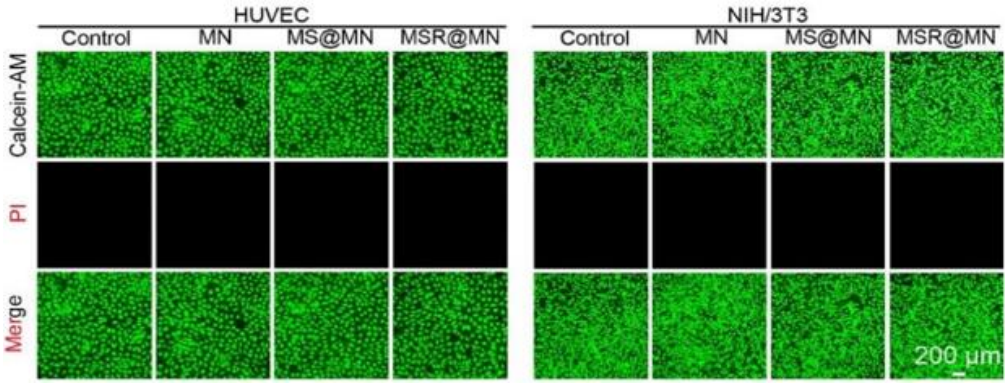

b)

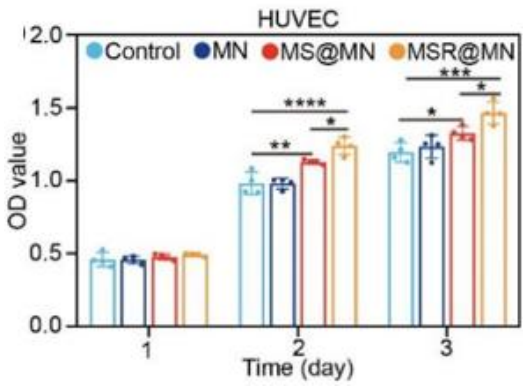

c)

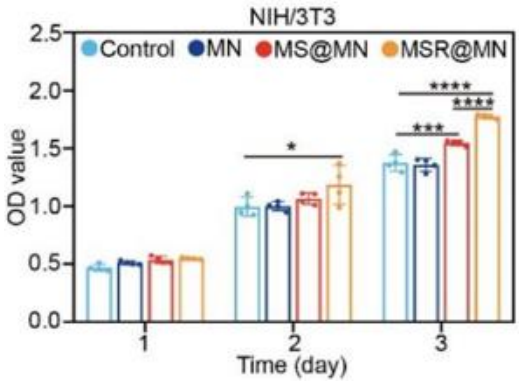

d)

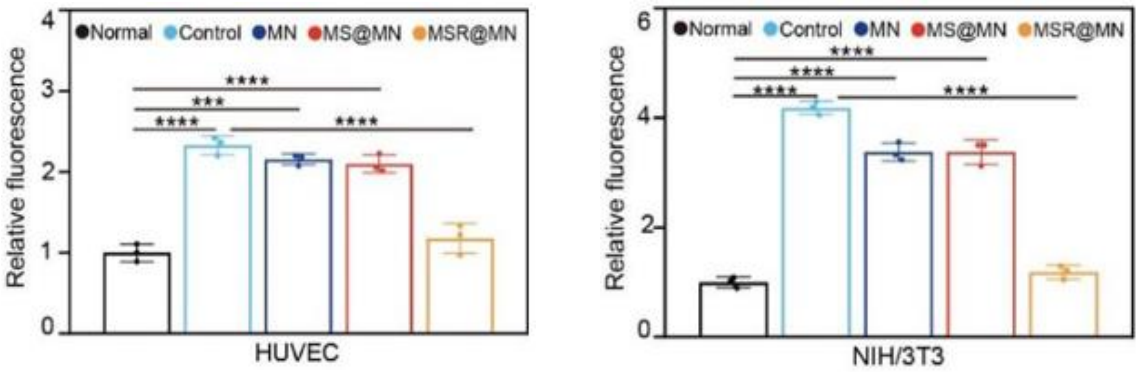

e) f)

Figure 4. In vitro bioapplications of MSR@MN. (a) Intracellular reactive oxygen species (ROS) scavenging efficacy of MSR@MN in human umbilical vein endothelial cells (HUVECs) and NIH/3T3 cells. (b) Live/dead staining and (c–d) cell proliferation assays of HUVECs and NIH/3T3 cells. (e, f) Quantitative analysis of relative ROS fluorescence intensity across treatment groups.

Subsequent evaluation of in vitro cytotoxicity was performed on HUVECs and NIH/3T3 cells using live/dead staining. High cell viability was observed across all treatment groups, confirming the low cytotoxicity of MSR@MN **(Figure 4b)**. To further assess proliferative capacity, CCK-8 assays were conducted. Cell proliferation was significantly enhanced in both the MS@MN and MSR@MN groups relative to other treatments on days 2 and 3 **(Figures 4c and 4d)**. These findings highlight the excellent biocompatibility of MSR@MN and its ability to support cell growth.

Blood compatibility was additionally examined through hemolysis assays, a standard metric for biomaterial safety. The MN, MS@MN, and MSR@MN patches produced clear supernatants with hemolysis ratios below 4%, indicating high hemocompatibility. Overall, these data demonstrate that MSR@MN exhibits favorable blood compatibility under in vitro conditions.

Cell migration and angiogenesis in vitro

Cell migration and the formation of new blood vessels are fundamental processes that occur during the early phases of wound repair [46, 47]. Previous investigations have indicated that magnesium ions can enhance cellular motility and growth, thereby supporting neovascularization and expediting tissue regeneration. The migratory behavior of human umbilical vein endothelial cells (HUVECs) was evaluated through scratch wound healing and Transwell chamber assays **(Figures 5a and 5b)**. Following 24 h of treatment, the percentage of wound closure reached 37.8 ± 3.7%, 42.3 ± 2.1%, 68.9 ± 3.3%, and 86.2 ± 2.1% in the Control, MN, MS@MN, and MSR@MN groups, respectively **(Figure 5d)**. Consistent trends were noted in parallel experiments with NIH/3T3 fibroblasts. In the Transwell system, both MS@MN and MSR@MN treatments led to a pronounced increase in the number of cells that traversed the membrane compared with the other groups. Detailed quantification showed that MSR@MN enhanced HUVEC migration by a factor of 4.2 relative to the untreated control **(Figure 5e)**.

A Matrigel-based tube formation assay was additionally performed to determine the impact of the materials on the angiogenic capacity of HUVECs **(Figure 5c)**. The extent of vascular network development was quantified by counting the number of branch points **(Figure 5f)** and measuring the overall length of capillary-like structures. MSR@MN treatment resulted in markedly improved tube assembly and network complexity compared with the control. Furthermore, the MSR@MN group demonstrated a 10.7% higher angiogenic response than the MS@MN group. Overall, these in vitro findings establish that MSR@MN strongly stimulates endothelial cell migration and tubulogenesis, highlighting its potential to promote angiogenesis and support wound healing processes in vivo.

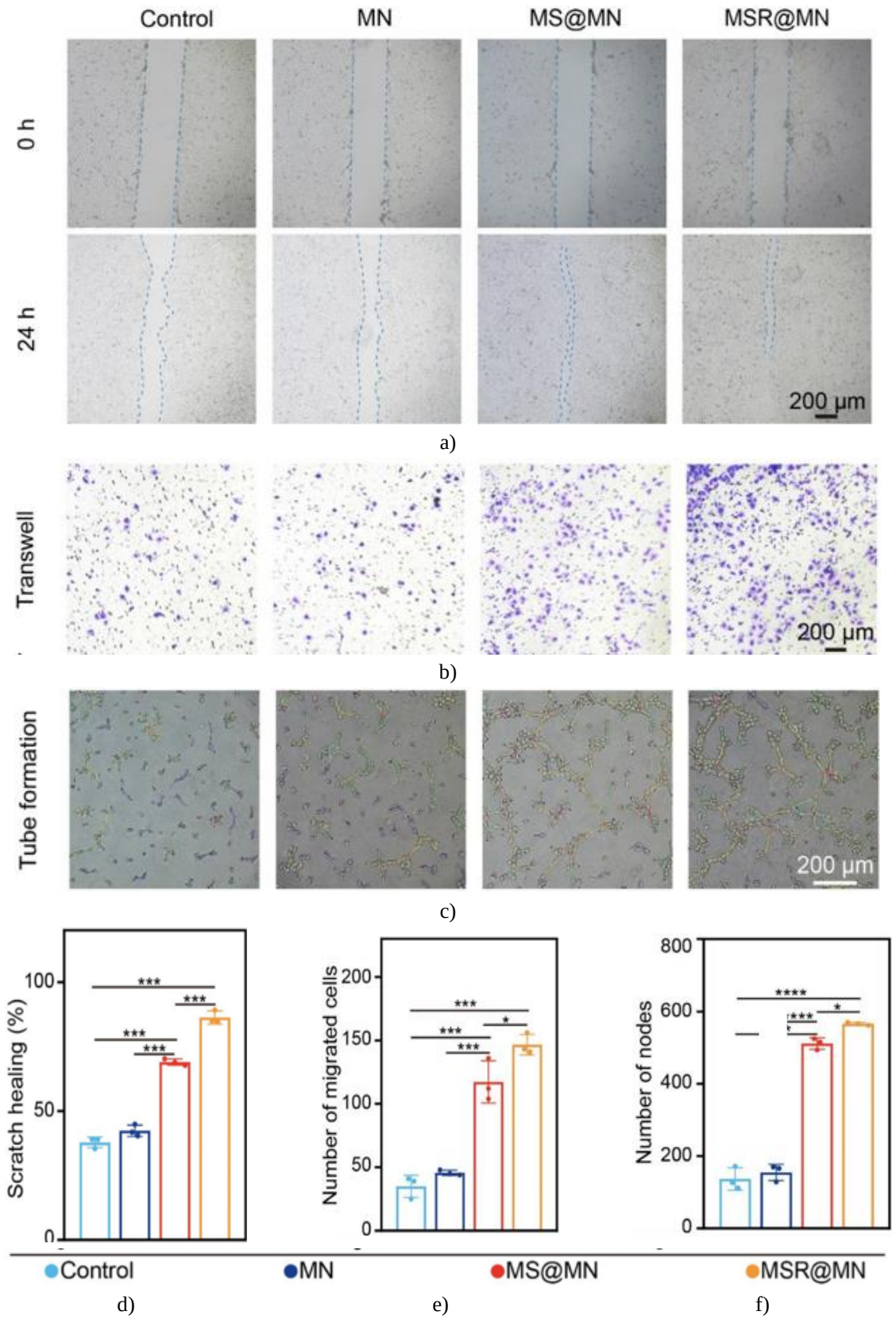

Figure 5. In vitro evaluation of cell migration and angiogenesis. (a) Representative images from the scratch assay. (b) Images of cells that migrated through the Transwell membrane. (c) Microscopic images showing tubule formation by human umbilical vein endothelial cells (HUVECs) in various treatment groups. (d) Quantitative assessment of HUVEC wound closure (n = 3). (e) Count of migrated cells following 24 h incubation (n = 3). (f) Number of nodes observed in randomly chosen microscopic fields (n = 3). Data represent mean ± SD; *p < 0.05, **p < 0.01, ***p < 0.001, ****p < 0.0001.

In vivo wound healing of radiation-induced skin defects

A considerable number of patients receiving radiation therapy develop skin reactions ranging from erythema and desquamation to more severe manifestations such as edema and ulceration [48]. Timely and effective management of these complications is essential. Although various protective measures exist, some patients still suffer progressive skin injury that results in open defects. In such cases, radiotherapy is often interrupted to avoid infection and tissue necrosis, with resumption delayed until sufficient healing occurs. Animal models serve as critical tools for replicating pathological processes and testing potential treatments. Nevertheless, no standardized protocol has been universally adopted for establishing radiation-induced skin defect models, particularly regarding radiation source, animal species, irradiation parameters, and anatomical site [49]. Most existing models rely on direct exposure of rodents using dedicated small-animal irradiators. To better simulate clinical radiotherapy-induced skin defects, the present study employed clinical linear accelerators to irradiate the dorsal skin of mice. Following the development of secondary skin damage, the irradiated area was excised to generate a clinically relevant radiation-induced skin defect model **(Figure 6a)**. This methodology seeks to improve translational relevance between preclinical studies and patient care, aiding the advancement of targeted therapies for radiation-related skin injuries.

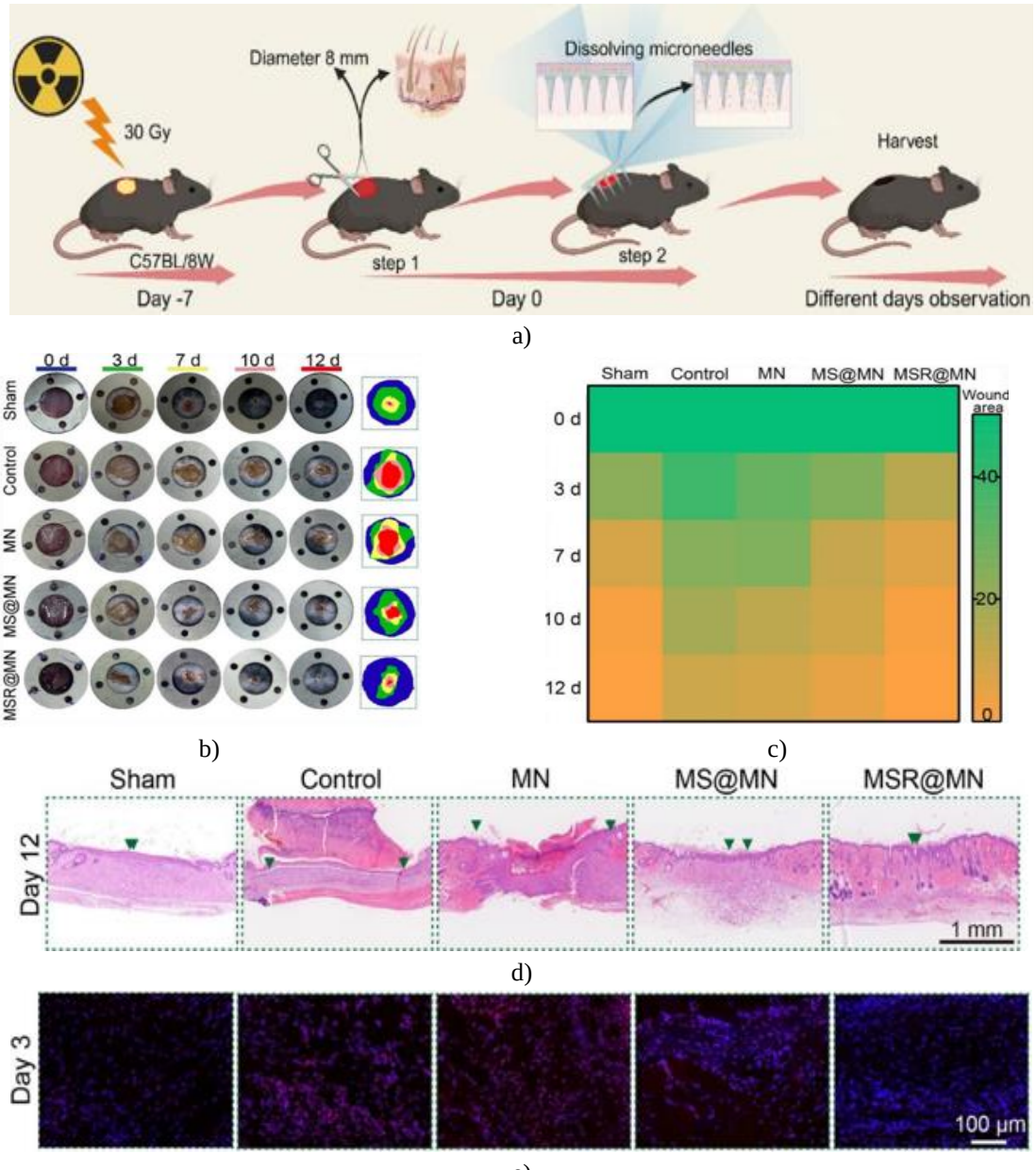

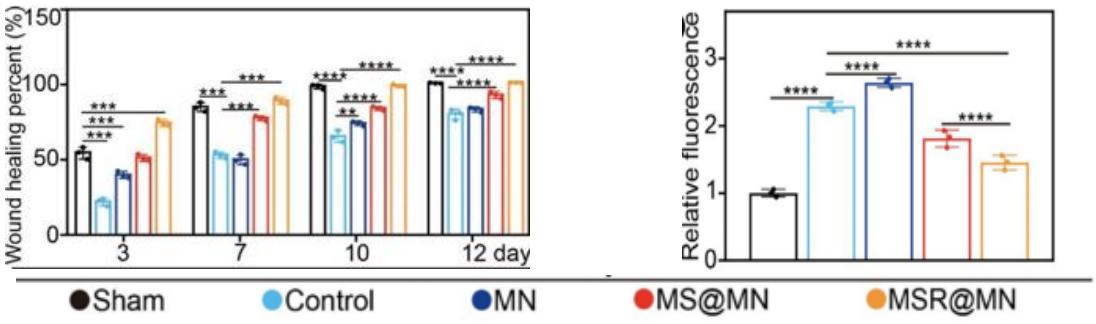

f) g)

Figure 6. MSR@MN modulates the complete repair process of radiotherapy-induced skin defects (RISD) in mice. (a) Schematic overview of the experimental workflow. (b) Representative photographs documenting wound closure in different treatment groups. (c) Quantitative analysis of relative wound area over time (n = 3). (d) Hematoxylin and eosin (H&E) staining of wound sections from various groups on day 12. (e) Immunofluorescence detection of reactive oxygen species (ROS) in wound tissue on day 3. (f) Quantitative wound closure rates at different time points (n = 3). (g) Semi-quantitative analysis of ROS fluorescence intensity on day 3 (n = 3). Data are expressed as mean ± SD; *p < 0.05, **p < 0.01, ***p < 0.001, ****p < 0.0001.

Immediately after application (Day 0), the microneedle patch adhered securely to the wound surface, with the needle tips successfully penetrating the skin. Upon insertion, the γ-PGA matrix dissolved rapidly, releasing the embedded therapeutic components into the dermal layers while the patch backing maintained a protective, moist environment that promotes healing. Wound progression was documented photographically at predefined intervals. By Day 7, the MS@MN and MSR@MN groups achieved wound closure rates of approximately 76.5% and 87.6%, respectively, outperforming the Control group (52.8%). No significant difference was detected between the MSR@MN and Sham groups (83.7%). By Day 12, wounds in both MS@MN and MSR@MN groups were almost completely closed, with the MSR@MN treatment yielding the best cosmetic outcome and minimal scar formation. In contrast, the Control group retained visible open areas and crusting **(Figure 6b)**. Wound area measurements further confirmed the accelerated healing kinetics in the MSR@MN group compared with the Control **(Figures 6c and 6f)**. Histological evaluation using H&E staining on Day 12 revealed granulation tissue in all groups, with more advanced tissue filling observed in the Sham and MSR@MN specimens **(Figure 6d)**. Notably, MSR@MN-treated wounds displayed newly formed epidermal ridges and hair follicles, indicating superior structural and functional restoration. Histological examination of major organs (heart, lung, liver, spleen, and kidney) showed no detectable toxicity across groups. Additionally, hematological parameters and serum biochemical markers remained comparable before and after treatment, supporting the good biocompatibility of the materials.

While physiological levels of ROS help maintain cellular signaling and tissue homeostasis [50], excessive ROS generated by irradiation disrupts these pathways and impedes wound repair. To evaluate the ROS-scavenging performance of MSR@MN in vivo, immunofluorescence staining was conducted on wound tissues collected on Day 3. Intense red fluorescence was evident in the Control group, reflecting high ROS accumulation. In comparison, both MS@MN and MSR@MN groups exhibited reduced fluorescence, with the MSR@MN treatment producing the most substantial decrease, indicative of superior ROS neutralization and improved tissue recovery **(Figure 6e)**. Semi-quantitative analysis corroborated these observations **(Figure 6g)**. Interestingly, the MS@MN group also displayed a noticeable reduction in ROS levels, albeit less pronounced than MSR@MN, suggesting inherent antioxidant potential of the MS component. Although ROS levels in the MSR@MN group were the lowest, they did not fully return to baseline (Sham group), implying that additional bioactive elements in MSR@MN contribute to later stages of wound healing. These results highlight the multifaceted therapeutic mechanisms of MSR@MN in managing radiation-induced skin wounds.

Histopathologic evaluations of radiotherapy-induced skin defect healing with MSR@MN treatment in mice

Successful restoration of redox balance within the wound microenvironment establishes favorable conditions for the skin's intrinsic regenerative processes. These processes involve an orderly progression through inflammatory, proliferative, and remodeling phases [51].

During the early inflammatory phase, pro-inflammatory M1 macrophages play a central role in pathogen clearance and wound debridement. These cells subsequently transition into anti-inflammatory M2 macrophages, which release cytokines that support tissue repair. Interference with this M1-to-M2 phenotypic switch can prolong inflammation and stall the healing cascade [52]. Immunofluorescence analysis revealed a progressive reduction in CD68 (M1 marker) expression alongside increased CD206 (M2 marker) levels in both the MS@MN and MSR@MN groups. These changes indicate that the treatments effectively promote timely macrophage polarization from the pro-inflammatory M1 phenotype toward the pro-healing M2 phenotype **(Figures 7a, 7e and 7f)**, thereby advancing the wound healing sequence.

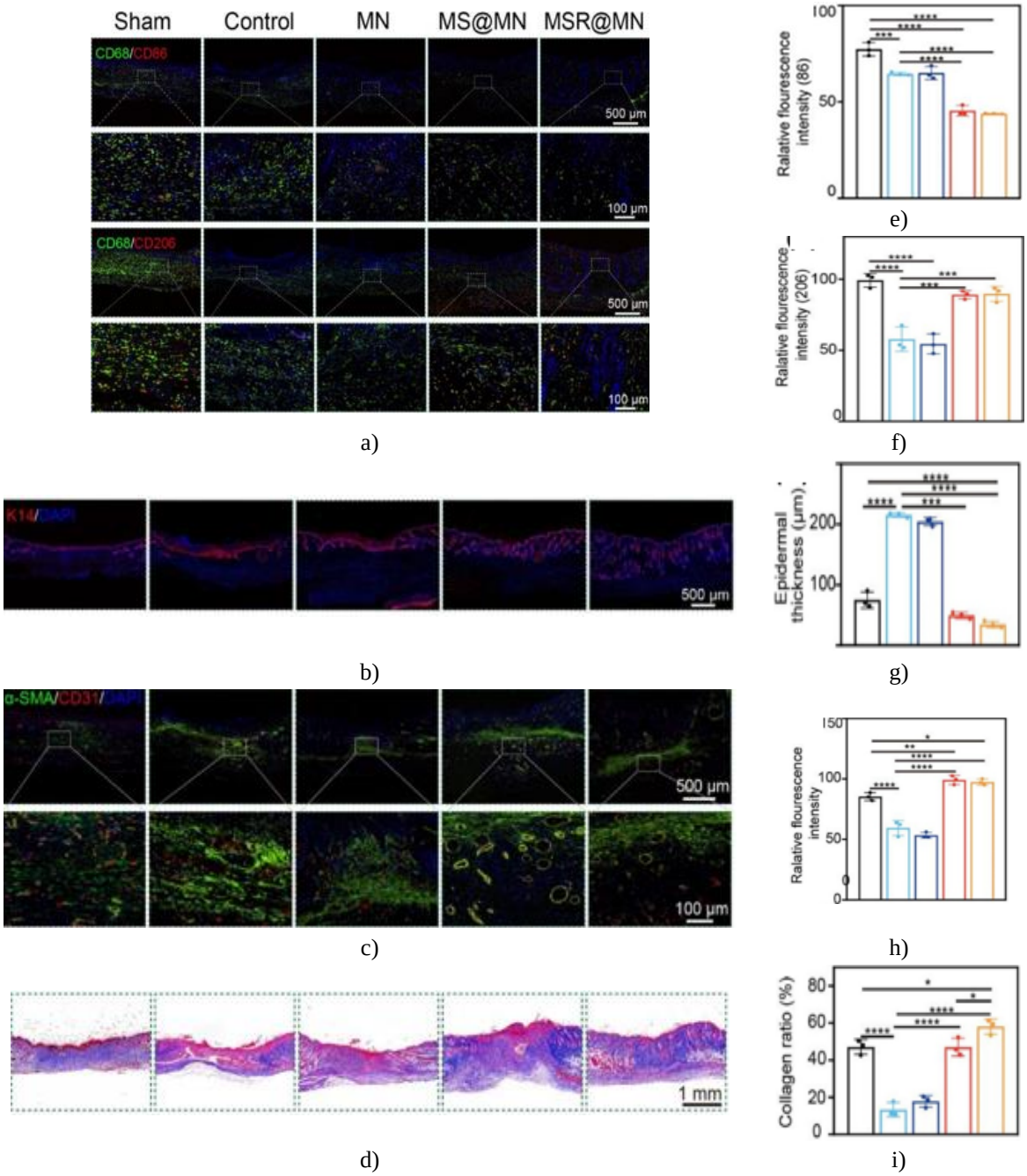

Figure 7. Skin regeneration in radiotherapy-induced skin defects (RISD). (a) Immunofluorescence staining for CD68/CD86 and CD206 on day 12. (b) Immunofluorescence staining for K14. (c) Immunofluorescence images of α-SMA (red) and CD31 (green) on day 12 after different treatments. (d) Masson's trichrome staining of wound sections from various groups. (E–F) Quantitative relative fluorescence intensity of (e) CD86 and (f) CD206. (g) Epidermal thickness measurement. (h–i) Quantitative analysis of (h) α-SMA and (i) collagen content. Data represent mean ± SD; *p < 0.05, **p < 0.01, ***p < 0.001, ****p < 0.0001.

Immunofluorescence staining was further utilized to examine the epithelial marker K14. The Control group displayed elevated K14 expression and increased epidermal thickness. In contrast, the MS@MN and MSR@MN groups showed reduced K14 levels and thinner epidermis, accompanied by the formation of hair follicles and epidermal ridges—most prominently in the MSR@MN group. These features suggest that wounds in the Control group remained in the re-epithelialization or proliferative phase, whereas the MS@MN and MSR@MN groups had advanced to the remodeling phase, evidenced by the regeneration of skin appendages that restore normal skin architecture. Notably, the Sham group lacked hair follicles and epidermal ridges compared with the MSR@MN group, highlighting the superior ability of MSR@MN to drive progression from epithelialization to full remodeling and functional skin restoration **(Figures 7band 7g)**.

The remodeling phase involves maturation of vasculature, regression of immature capillaries, and organized collagen deposition. To evaluate neovascularization, co-staining for CD31 and α-SMA was performed. While the Control group showed abundant immature capillaries, the MS@MN and MSR@MN groups exhibited mature, functional blood vessels. Semi-quantitative analysis confirmed enhanced angiogenesis in these treatment groups **(Figures 7c and 7h)**. Collagen deposition, particularly type I collagen, was assessed using Masson's trichrome staining. Both MS@MN and MSR@MN groups displayed dermal architecture resembling normal skin, with MSR@MN producing the most extensive collagen deposition. Collagen volume fractions were quantified as 47.1 ± 3.2%, 13.4 ± 0.3%, 17.9 ± 2.5%, 47.1 ± 3.8%, and 58.1 ± 2.3% for the Sham, Control, MN, MS@MN, and MSR@MN groups, respectively **(Figures 7d and 7i)**. These results demonstrate that MS@MN and MSR@MN treatments effectively promote tissue remodeling by enhancing vascular maturation and collagen organization.

Mechanism exploration of wound healing-related biological processes

To investigate the molecular basis responsible for the therapeutic action of MSR@MN, RNA sequencing (RNA-seq) was carried out on wound tissue specimens obtained on Day 12, using untreated wounds as the Control. Principal component analysis revealed distinct transcriptional profiles between the Control and MSR@MN groups **(Figure 8a)**. Comparative analysis identified a total of 1141 differentially expressed genes (DEGs), of which 655 were upregulated and 486 downregulated. These alterations are depicted in volcano plots and heatmaps **(Figures 8b and 8c)**.

Functional annotation through Gene Ontology and Kyoto Encyclopedia of Genes and Genomes (KEGG) pathway analyses indicated significant enrichment of the DEGs in key biological processes and signaling cascades, including regulation of angiogenesis, wound healing responses, modulation of inflammatory reactions, control of cytosolic calcium levels, epidermal development, and positive regulation of receptor-mediated signaling. The peroxisome proliferator-activated receptor (PPAR) signaling pathway stood out as particularly relevant, given its established involvement in managing intracellular free radical levels **(Figure 8d)**. PPAR signaling exerts broad regulatory influence over inflammation, immune function, cell proliferation, differentiation, and growth [53-55]. It also enhances expression of mitochondrial uncoupling protein 2 (UCP2), contributing to the maintenance of ROS homeostasis [56]. Consistent with these pathway enrichments, Western blot experiments demonstrated increased expression of PPAR and UCP2 proteins in tissues treated with MSR@MN **(Figure 8e)**. This suggests that MSR@MN operates through dual mechanisms: direct elimination of preexisting ROS and suppression of their intracellular generation.

Gene set enrichment analysis (GSEA) additionally highlighted activation of the calcium signaling pathway, along with enhanced calcium ion transmembrane transport and release of stored calcium into the cytosol **(Figure 8f)**. In parallel, notable suppression was observed in intrinsic apoptotic pathways, cysteine-type endopeptidase activity associated with apoptosis, and IL-17 signaling **(Figures 8g–8i)**. These pathways are intimately connected with the inflammatory and proliferative stages of wound repair. Quantitative real-time PCR analysis independently validated the elevated expression of several critical wound healing-associated genes in the MSR@MN group.

In summary, the collective findings indicate that MSR@MN robustly activates and coordinates multiple biological pathways essential for effective wound healing, thereby demonstrating strong potential as a regenerative therapeutic platform.

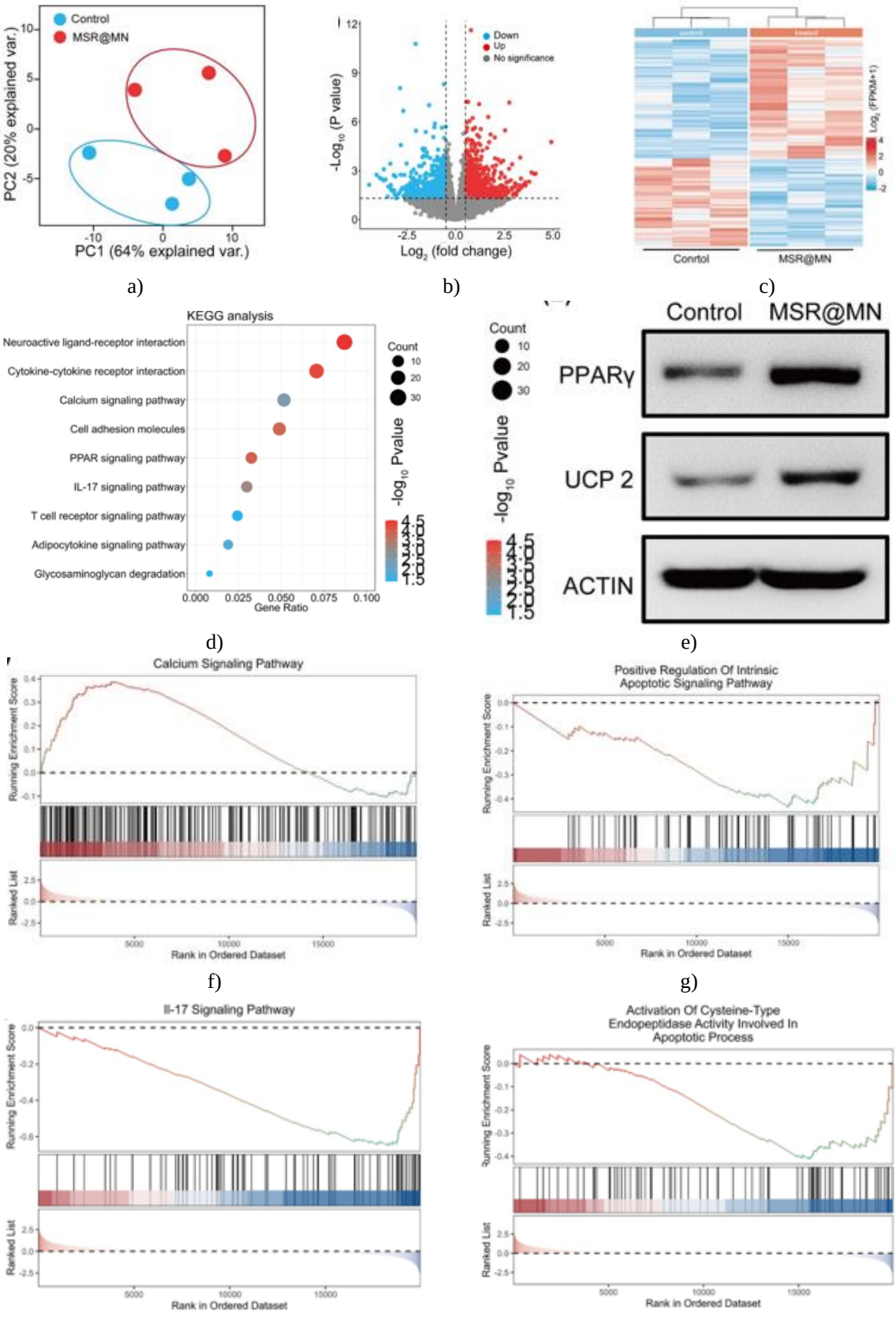

Figure 8. RNA sequencing (RNA-seq) analysis. (a) Principal component analysis (PCA) demonstrating transcriptional differences between the Control and MSR@MN groups. (b and c) Volcano plot and heatmap displaying differentially expressed genes (DEGs), where red dots denote upregulated genes and blue dots represent downregulated genes. (d) Kyoto Encyclopedia of Genes and Genomes (KEGG) pathway

enrichment results. (e) Western blot detection of central proteins within the enriched pathways for Control versus MSR@MN groups. (f to i) Gene set enrichment analysis (GSEA) for pathways and processes associated with inflammation, apoptosis, and proliferation.

Comparison among γPGA-MSR ointment and commercial products in mice

To thoroughly validate the therapeutic performance of MSR@MN in radiation-induced skin damage (RISD), two positive control groups were included in the in vivo experiments: a γPGA-MSR ointment and the commercially available Orgotein preparation. Both the γPGA-MSR ointment and MSR@MN treatments achieved markedly higher wound closure rates than the remaining groups, with MSR@MN demonstrating the greatest efficacy. This outcome emphasizes the benefit of microneedle-mediated delivery for targeted and efficient local drug administration. By Day 7, the MSR@MN group exhibited significantly faster healing compared with both the Control and commercial product groups, with the difference becoming more pronounced by Day 12 **(Figures 9a and 9b)**. Immunofluorescence staining for ROS further showed that MSR@MN, γPGA-MSR ointment, and Orgotein all displayed effective ROS-scavenging activity. However, MSR@MN achieved slightly superior ROS reduction relative to the commercial formulation **(Figures 9c and 9f)**. These observations collectively highlight MSR@MN as a highly promising approach that combines efficient localized delivery with potent antioxidant activity to improve wound healing outcomes.

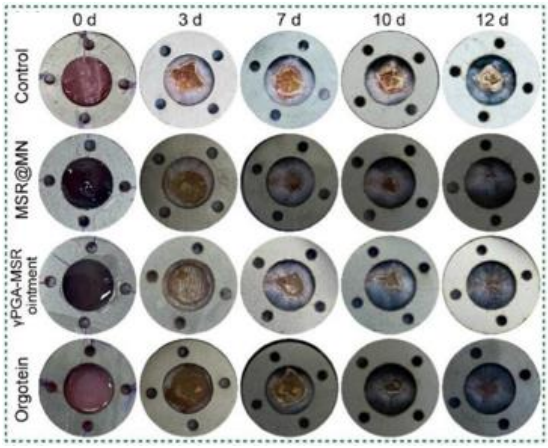

a)

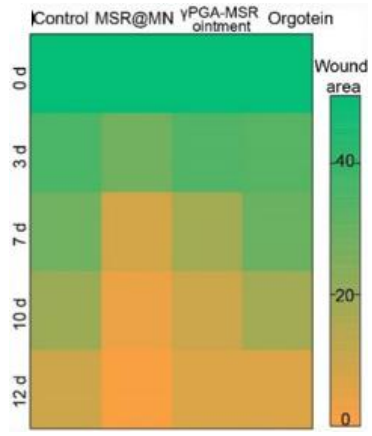

b)

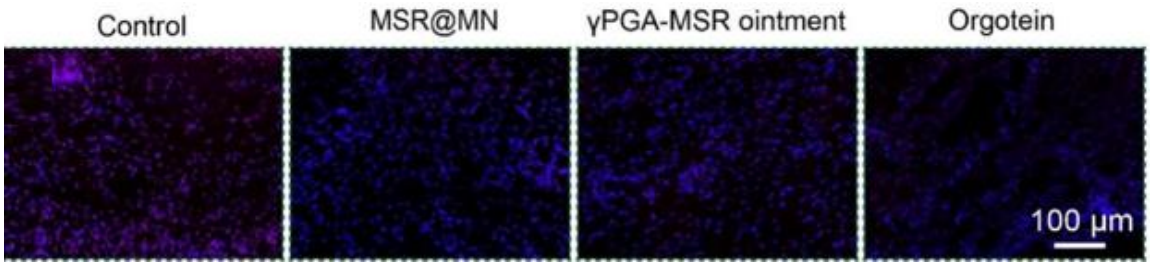

c)

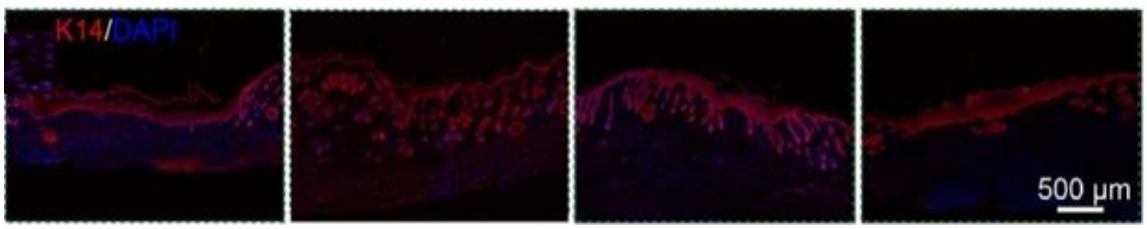

d)

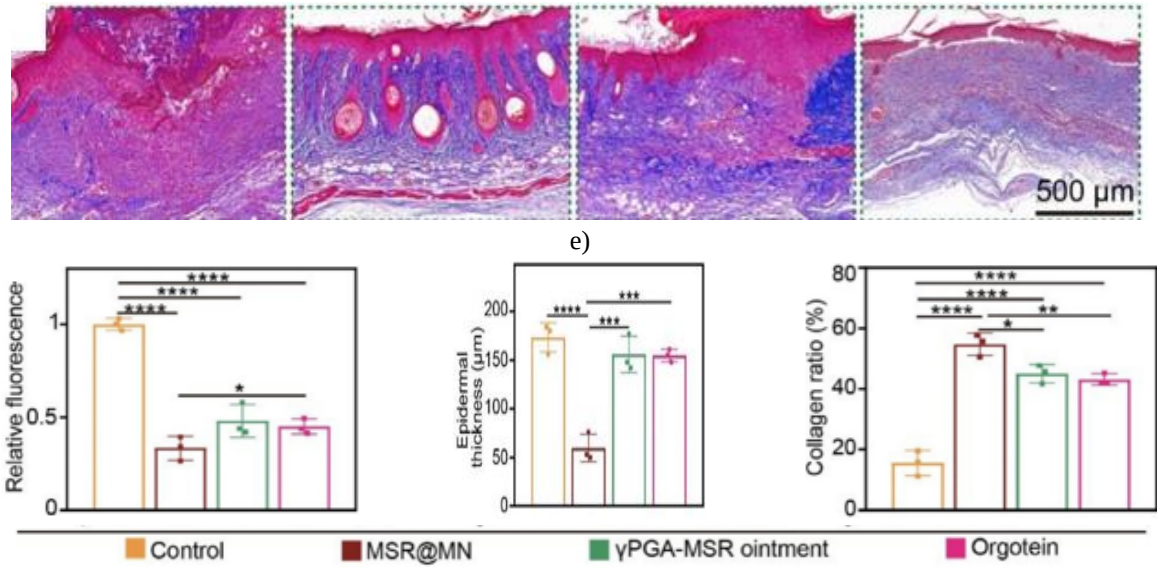

Figure 9. MSR@MN and commercial products in the regulation of radiotherapy-induced skin defect (RISD) repair in mice. (a) Representative photographs of wound healing progression across treatment groups. (b) Quantitative assessment of relative wound area at indicated time points (n = 3). (c) Immunofluorescence detection of reactive oxygen species (ROS) in wound tissue on day 3. (d) Immunofluorescence staining for K14. (e) Masson's trichrome staining of wound sections from different groups. (f) Quantitative relative fluorescence intensity of ROS on day 3 (n = 3). (g) Measurement of epidermal thickness. (h) Quantitative analysis of collagen content. *p < 0.05, **p < 0.01, ***p < 0.001, ****p < 0.0001.

With respect to re-epithelialization, both MSR@MN and γPGA-MSR ointment promoted robust epidermal regeneration, with MSR@MN showing the strongest effect. Although Orgotein also supported epithelial recovery, it failed to induce the formation of skin appendages such as hair follicles **(Figures 9d and 9g)**. This limitation may arise because its primary active ingredient, superoxide dismutase, lacks additional bioactive components that facilitate comprehensive tissue repair. Corresponding hematoxylin and eosin (H&E) staining images confirmed more advanced epidermal regeneration in the MSR@MN group compared with the Control, γPGA-MSR ointment, and Orgotein groups on day 12.

Angiogenesis and collagen deposition were also evaluated. While all treatments enhanced new vessel formation relative to the Control, MSR@MN and γPGA-MSR ointment groups were superior in promoting the maturation of fully functional blood vessels. In contrast, vessels in the commercial product group remained predominantly in an immature state. Regarding collagen deposition—a key indicator of healing progression—the MSR@MN group displayed the highest collagen content, significantly exceeding the other treatment and Control groups, although all active treatments increased collagen levels **(Figures 9e and 9h)**. These results demonstrate the clear advantages of MSR@MN over existing commercial options, especially in supporting the regeneration of skin appendages and mature tissue structures.

Conclusion

In conclusion, a multifunctional composite microneedle (MN) patch was developed for the management of radiotherapy-induced skin defects (RISD). This system provides immediate ROS scavenging, subsequent suppression of ROS generation, and modulation of proliferation-related signaling pathways. The patch was fabricated using γ-PGA as the matrix combined with ruthenium cluster-modified magnesium silicate nanosheets (MSR NSs) as the bioactive component through a solvent-assisted process, thermal reduction, and mold-casting technique. The resulting MSR material exhibited broad-spectrum free radical scavenging activity attributable to the strong reductive capacity of the Ru clusters, which effectively supports initial ROS clearance and anti-inflammatory responses during skin repair. In vitro studies demonstrated that MSR enhances cell proliferation, migration, and tubule formation, effects primarily linked to the release of bioactive magnesium and silicate ions. A clinically relevant radiation-induced skin defect model in mice was established to compare the performance of

the MSR@MN dressing against γPGA-MSR ointment and the commercial Orgotein product. In vivo results revealed that MSR@MN promoted greater collagen deposition (exceeding 20%), accelerated re-epithelialization, and faster restoration of normal skin architecture, as evidenced by mature vasculature and hair follicle regeneration, while shortening overall healing time by approximately 13%. High-throughput RNA sequencing further indicated significant enrichment of the PPAR signaling pathway in MSR@MN-treated tissues, which contributes to mitochondrial ROS suppression and restoration of normal cellular functions. Collectively, these findings indicate that the MSR@MN patch accelerates wound healing through simultaneous attenuation of oxidative stress and reactivation of disrupted cellular signaling networks.

Acknowledgments: None

Conflict of Interest: None

Financial Support: None

Ethics Statement: None

References

1. Ruhlmann CH, Jahn F, Jordan K, Dennis K, Maranzano E, Molassiotis A, et al. 2016 updated MASCC/ESMO consensus recommendations: prevention of radiotherapy-induced nausea and vomiting. Support Care Cancer. 2017;25(1):309-16. doi:10.1007/s00520-016-3370-4
2. Dasgupta Q, Jiang A, Wen AM, Mannix RJ, Man Y, Hall S, et al. A human lung alveolus-on-a-chip model of acute radiation-induced lung injury. Nat Commun. 2023;14:6506. doi:10.1038/s41467-023-42171-z
3. Gomez-Millan J. Radiation therapy in the elderly: more side effects and complications? Crit Rev Oncol Hematol. 2009;71(1):70-8. doi:10.1016/j.critrevonc.2008.11.004
4. Ha DH, Chae S, Lee JY, Kim JY, Yoon J, Sen T, et al. Therapeutic effect of decellularized extracellular matrix-based hydrogel for radiation esophagitis by 3D printed esophageal stent. Biomaterials. 2021;266:120477. doi:10.1016/j.biomaterials.2020.120477
5. Zhang Z, Cao Q, Xia Y, Cui C, Qi Y, Zhang Q, et al. Combination of biodegradable hydrogel and antioxidant bioadhesive for treatment of breast cancer recurrence and radiation skin injury. Bioact Mater. 2024;31:408-21. doi:10.1016/j.bioactmat.2023.08.015
6. Chen W, Wang Y, Zheng J, Chen Y, Zhang C, Yang W, et al. Characterization of cellular senescence in radiation ulcers and therapeutic effects of mesenchymal stem cell-derived conditioned medium. Burns Trauma. 2023;11:tkad001. doi:10.1093/burnst/tkad001
7. Wang Z, Chen Z, Jiang Z, Luo P, Liu L, Huang Y, et al. Cordycepin prevents radiation ulcer by inhibiting cell senescence via NRF2 and AMPK in rodents. Nat Commun. 2019;10:2538. doi:10.1038/s41467-019-10586-y
8. Xie J, Zhao M, Wang C, Zhu S, Niu W, Yong Y, et al. Nano-graphdiyne hydrogel for skin radioprotection via both physically shielding of low-energy X-ray and chemically scavenging of broad-spectrum free radicals. Chem Eng J. 2022;430:132866. doi:10.1016/j.cej.2021.132866
9. Fang Z, Lv Y, Zhang H, He Y, Gao H, Chen C, et al. A multifunctional hydrogel loaded with two nanoagents improves the pathological microenvironment associated with radiation combined with skin wounds. Acta Biomater. 2023;159:111-27. doi:10.1016/j.actbio.2023.01.052
10. Hass DT, Barnstable CJ. Uncoupling proteins in the mitochondrial defense against oxidative stress. Prog Retin Eye Res. 2021;83:100941. doi:10.1016/j.preteyeres.2021.100941
11. Smolarz M, Skoczylas Ł, Gawin M, Krzyżowska M, Pietrowska M, Widłak P. Radiation-induced bystander effect mediated by exosomes involves the replication stress in recipient cells. Int J Mol Sci. 2022;23(8):4169. doi:10.3390/ijms23084169
12. Geng F, Chen J, Song B, Tang Z, Li X, Zhang S, et al. Chaperone- and PTM-mediated activation of IRF1 tames radiation-induced cell death and the inflammatory response. Cell Mol Immunol. 2024;21(8):856-72. doi:10.1038/s41423-024-01185-3

13. Ge J, Jia B, Wang Y, Ma Y, Sun X, Dong J, et al. DNA nanostructures treat inflammatory bowel disease through ROS scavenging and gut microbiota modulation. Adv Funct Mater. 2024;34:2402781. doi:10.1002/adfm.202402781
14. Liu J, Dong Y, Tang J, Wu J, Huang Y, Yao C, et al. A DNA nanocomplex with bifunctions of reactive oxygen species scavenging and gene silencing for synergistic repair of myocardial infarction. Nano Today. 2024;55:102185. doi:10.1016/j.nantod.2024.102185
15. Zheng Y, Chen X, Zhang Q, Yang L, Chen Q, Chen Z, et al. Evaluation of reactive oxygen species scavenging of polydopamine with different nanostructures. Adv Healthc Mater. 2024;13(4):e2302640. doi:10.1002/adhm.202302640
16. Guo Y, Ding S, Shang C, Zhang C, Li M, Zhang Q, et al. Multifunctional PtCuTe nanosheets with strong ROS scavenging and ROS-independent antibacterial properties promote diabetic wound healing. Adv Mater. 2024;36(8):e2306292. doi:10.1002/adma.202306292
17. Liu J, Chen Z, Liu H, Qin S, Li M, Shi L, et al. Nickel-based metal-organic frameworks promote diabetic wound healing via scavenging reactive oxygen species and enhancing angiogenesis. Small. 2023;20:2305076. doi:10.1002/smll.202305076
18. Xu Y, Luo Y, Weng Z, Xu H, Zhang W, Li Q, et al. Microenvironment-responsive metal-phenolic nanozyme release platform with antibacterial, ROS scavenging, and osteogenesis for periodontitis. ACS Nano. 2023;17(19):18732-46. doi:10.1021/acsnano.3c01940
19. Zhang W, Zhao M, Chu D, Chen H, Cui B, Ning Q, et al. Dual-ROS-scavenging and dual-lingering nanozyme-based eye drops alleviate dry eye disease. J Nanobiotechnol. 2024;22(1):229. doi:10.1186/s12951-024-02499-0
20. Lian M, Xue Z, Qiao X, Liu C, Zhang S, Li X, et al. Movable hollow nanoparticles as reactive oxygen scavengers. Chem. 2019;5(9):2378-87. doi:10.1016/j.chempr.2019.05.023
21. Huang HM, Bellotti P, Ma J, Dalton T, Glorius F. Bifunctional reagents in organic synthesis. Nat Rev Chem. 2021;5:301-21. doi:10.1038/s41570-021-00272-7
22. Li J, Zeng L, Wang Z, Chen H, Fang S, Wang J, et al. Cycloruthenated self-assembly with metabolic inhibition to efficiently overcome multidrug resistance in cancers. Adv Mater. 2022;34(1):e2100245. doi:10.1002/adma.202100245
23. Shi CY, Chen XQ, Zeng R, Lu H, Fan Z, Zhang A. Ruthenium-catalyzed ligand-enabled regiodivergent difluoroallylation of aryl C–H bonds. Org Lett. 2023;25(21):3870-5. doi:10.1021/acs.orglett.3c00873
24. Song Y, Min J, Guo Y, Li R, Zou G, Li M, et al. Surface activation by single Ru atoms for enhanced high-temperature CO2 electrolysis. Angew Chem Int Ed. 2024;63:e202313361. doi:10.1002/anie.202313361
25. Wang B, Fang Y, Han X, Jiang R, Zhao L, Yang X, et al. Atomization-induced high intrinsic activity of a biocompatible MgAl-LDH supported Ru single-atom nanozyme for efficient radicals scavenging. Angew Chem Int Ed. 2023;62(38):e202307133. doi:10.1002/anie.202307133
26. Liu C, Rokavec M, Huang Z, Hermeking H. Curcumin activates a ROS/KEAP1/NRF2/miR-34a/b/c cascade to suppress colorectal cancer metastasis. Cell Death Differ. 2023;30:1771-85. doi:10.1038/s41418-023-01191-6
27. Liu X, Zhao P, Wang X, Wang L, Zhu Y, Song Y, et al. Celastrol mediates autophagy and apoptosis via the ROS/JNK and Akt/mTOR signaling pathways in glioma cells. J Exp Clin Cancer Res. 2019;38:184. doi:10.1186/s13046-019-1188-2
28. Cao F, Jin L, Gao Y, Ding Y, Wen H, Qian Z, et al. Artificial-enzymes-armed Bifidobacterium longum probiotics for alleviating intestinal inflammation and microbiota dysbiosis. Nat Nanotechnol. 2023;18:617-27. doi:10.1038/s41565-023-01369-4
29. Curvino EJ, Roe EF, Freire Haddad H, Anderson AR, Woodruff ME, Votaw NL, et al. Engaging natural antibody responses for the treatment of inflammatory bowel disease via phosphorylcholine-presenting nanofibres. Nat Biomed Eng. 2024;8:628-49. doi:10.1038/s41551-023-01139-6
30. Fan Q, Yang Z, Li Y, Cheng Y, Li Y. Polycatechol mediated small interfering RNA delivery for the treatment of ulcerative colitis. Adv Funct Mater. 2021;31:2101646. doi:10.1002/adfm.202101646
31. Ege D, Zheng K, Boccaccini AR. Borate bioactive glasses (BBG): bone regeneration, wound healing applications, and future directions. ACS Appl Bio Mater. 2022;5:3608-20. doi:10.1021/acsabm.2c00384
32. Ma J, Wu C. Bioactive inorganic particles-based biomaterials for skin tissue engineering. Exploration. 2022;2(5):20210083. doi:10.1002/EXP.20210083

33. Fan C, Xu Q, Hao R, Wang C, Que Y, Chen Y, et al. Multi-functional wound dressings based on silicate bioactive materials. Biomaterials. 2022;287:121652. doi:10.1016/j.biomaterials.2022.121652
34. Xue J, Qin C, Wu C. 3D printing of cell-delivery scaffolds for tissue regeneration. Regen Biomater. 2023;10:rbad032. doi:10.1093/rb/rbad032
35. He H, Huang W, Zhang S, Li J, Zhang J, Li B, et al. Microneedle patch for transdermal sequential delivery of KGF-2 and aFGF to enhance burn wound therapy. Small. 2024;20(34):e2307485. doi:10.1002/smll.202307485
36. Li S, Wang X, Yan Z, Wang T, Chen Z, Song H, et al. Microneedle patches with antimicrobial and immunomodulating properties for infected wound healing. Adv Sci (Weinh). 2023;10(22):e2300576. doi:10.1002/advs.202300576
37. Lyu S, Dong Z, Xu X, Bei HP, Yuen HY, Cheung CWJ, et al. Going below and beyond the surface: microneedle structure, materials, drugs, fabrication, and applications for wound healing and tissue regeneration. Bioact Mater. 2023;27:303-26. doi:10.1016/j.bioactmat.2023.03.010
38. Allen BM, Hiam KJ, Burnett CE, Venida A, DeBarge R, Tenvooren I, et al. Systemic dysfunction and plasticity of the immune macroenvironment in cancer models. Nat Med. 2020;26(7):1125-34. doi:10.1038/s41591-020-0892-6
39. Tian YF, Li G, Xu DX, Lu ZY, Yan MY, Wan J, et al. Micrometer-sized SiMgyOx with stable internal structure evolution for high-performance Li-ion battery anodes. Adv Mater. 2022;34(15):e2200672. doi:10.1002/adma.202200672
40. Xia F, Hu X, Zhang B, Wang X, Guan Y, Lin P, et al. Ultrasmall ruthenium nanoparticles with boosted antioxidant activity upregulate regulatory T cells for highly efficient liver injury therapy. Small. 2022;18(29):e2201558. doi:10.1002/smll.202201558
41. Yin M, Wu J, Deng M, Wang P, Ji G, Wang M, et al. Multifunctional magnesium organic framework-based microneedle patch for accelerating diabetic wound healing. ACS Nano. 2021;15(11):17842-53. doi:10.1021/acsnano.1c06036
42. Sang M, Cho M, Lim S, Min IS, Han Y, Lee C, et al. Fluorescent-based biodegradable microneedle sensor array for tether-free continuous glucose monitoring with smartphone application. Sci Adv. 2023;9(22):eadh1765. doi:10.1126/sciadv.adh1765
43. Man J, Shen Y, Song Y, Yang K, Pei P, Hu L. Biomaterials-mediated radiation-induced diseases treatment and radiation protection. J Control Release. 2024;370:318-38.
44. Liu J, Shi L, Wang Y, Li M, Zhou C, Zhang L, et al. Ruthenium-based metal-organic framework with reactive oxygen and nitrogen species scavenging activities for alleviating inflammation diseases. Nano Today. 2022;47:101627. doi:10.1016/j.nantod.2022.101627
45. Sies H, Belousov VV, Chandel NS, Davies MJ, Jones DP, Mann GE, et al. Defining roles of specific reactive oxygen species (ROS) in cell biology and physiology. Nat Rev Mol Cell Biol. 2022;23(7):499-515. doi:10.1038/s41580-022-00456-z
46. Byun H, Han Y, Kim E, Jun I, Lee J, Jeong H, et al. Cell-homing and immunomodulatory composite hydrogels for effective wound healing with neovascularization. Bioact Mater. 2024;36:185-202. doi:10.1016/j.bioactmat.2024.02.029
47. Maldonado H, Savage BD, Barker HR, May U, Vähätupa M, Badiani RK, et al. Systemically administered wound-homing peptide accelerates wound healing by modulating syndecan-4 function. Nat Commun. 2023;14(1):8069. doi:10.1038/s41467-023-43848-1
48. Zhang J, Zhu Y, Zhang Y, Lin W, Ke J, Liu J, et al. A balanced charged hydrogel with anti-biofouling and antioxidant properties for treatment of irradiation-induced skin injury. Mater Sci Eng C. 2021;131:112538. doi:10.1016/j.msec.2021.112538
49. Hu Y, Miao Y, Zhang Y, Wang X, Liu X, Zhang W, et al. Co-assembled binary polyphenol natural products for the prevention and treatment of radiation-induced skin injury. ACS Nano. 2024;18(40):27557-69. doi:10.1021/acsnano.4c08508
50. Zhang J, Simpson CM, Berner J, Chong HB, Fang J, Ordulu Z, et al. Systematic identification of anticancer drug targets reveals a nucleus-to-mitochondria ROS-sensing pathway. Cell. 2023;186(11):2361-79.e25. doi:10.1016/j.cell.2023.04.026
51. Rodrigues M, Kosaric N, Bonham CA, Gurtner GC. Wound healing: a cellular perspective. Physiol Rev. 2019;99(1):665-706. doi:10.1152/physrev.00067.2017

52. Willenborg S, Sanin DE, Jais A, Ding X, Ulas T, Nüchel J, et al. Mitochondrial metabolism coordinates stage-specific repair processes in macrophages during wound healing. Cell Metab. 2021;33(12):2398-414.e9. doi:10.1016/j.cmet.2021.10.004
53. Konger RL, Derr-Yellin E, Zimmers TA, Katona T, Xuei X, Liu Y, et al. Epidermal PPARγ is a key homeostatic regulator of cutaneous inflammation and barrier function in mouse skin. Int J Mol Sci. 2021;22(16):8634. doi:10.3390/ijms22168634
54. Magadum A, Engel FB. PPARβ/δ: linking metabolism to regeneration. Int J Mol Sci. 2018;19(7):2013. doi:10.3390/ijms19072013
55. Zhong J, He X, Gao X, Liu Q, Zhao Y, Hong Y, et al. Hyodeoxycholic acid ameliorates nonalcoholic fatty liver disease by inhibiting RAN-mediated PPARα nucleus-cytoplasm shuttling. Nat Commun. 2023;14:5451. doi:10.1038/s41467-023-41180-2
56. Zhang X, Mao M, Zuo Z. Palmitate induces mitochondrial energy metabolism disorder and cellular damage via the PPAR signaling pathway in diabetic cardiomyopathy. Diabetes Metab Syndr Obes. 2022;15:2287-99. doi:10.2147/DMSO.S360931